Cancer Cell
Article

Metabolic Signatures Uncover Distinct Targets in Molecular Subsets of Diffuse Large B Cell Lymphoma

Pilar Caro,[1,10] Amar U. Kishan,[1,4,10] Erik Norberg,[1,5,10] Illana A. Stanley,[1,5] Bjoern Chapuy,[2] Scott B. Ficarro,[1,3,6] Klaudia Polak,[1] Daniel Tondera,[1] John Gounarides,[7] Hong Yin,[7] Feng Zhou,[1,3,6] Michael R. Green,[2] Linfeng Chen,[2] Stefano Monti,[8,9] Jarrod A. Marto,[1,3,6] Margaret A. Shipp,[2] and Nika N. Danial[1,5,*]

[1]Department of Cancer Biology
[2]Department of Medical Oncology
[3]Blais Proteomics Center
Dana-Farber Cancer Institute, Boston, MA 02115, USA
[4]Harvard-MIT Division of Health Sciences and Technology, Cambridge, MA 02139, USA
[5]Department of Cell Biology
[6]Department of Biological Chemistry and Molecular Pharmacology
Harvard Medical School, Boston, MA 02115, USA
[7]Novartis Institutes for Biomedical Research, Cambridge, MA 02139, USA
[8]The Broad Institute, Cambridge, MA 02142, USA
[9]Section of Computational Biomedicine, Boston University School of Medicine, Boston, MA 02218, USA
[10]These authors contributed equally to this work
*Correspondence: nika_danial@dfci.harvard.edu
http://dx.doi.org/10.1016/j.ccr.2012.08.014

SUMMARY

Molecular signatures have identified several subsets of diffuse large B cell lymphoma (DLBCL) and rational targets within the B cell receptor (BCR) signaling axis. The OxPhos-DLBCL subset, which harbors the signature of genes involved in mitochondrial metabolism, is insensitive to inhibition of BCR survival signaling but is functionally undefined. We show that, compared with BCR-DLBCLs, OxPhos-DLBCLs display enhanced mitochondrial energy transduction, greater incorporation of nutrient-derived carbons into the tricarboxylic acid cycle, and increased glutathione levels. Moreover, perturbation of the fatty acid oxidation program and glutathione synthesis proved selectively toxic to this tumor subset. Our analysis provides evidence for distinct metabolic fingerprints and associated survival mechanisms in DLBCL and may have therapeutic implications.

INTRODUCTION

Tumors often rewire their metabolism to ensure a steady supply of intermediary metabolites for synthesis of new biomass, as well as generation of ATP and reducing equivalents (Barger and Plas, 2010; DeBerardinis et al., 2008; Tennant et al., 2010). This metabolic reprogramming is a dynamic process shaped by oncogenes and tumor suppressors (Barger and Plas, 2010; Morrish et al., 2008; Yuneva et al., 2012). One of the first metabolic alterations identified in tumors is elevated glycolysis, even in the presence of sufficient oxygen. This program, also known as the Warburg effect or aerobic glycolysis, fulfills important biosynthetic needs (Barger and Plas, 2010; Koppenol et al., 2011; Vander Heiden et al., 2009). The Warburg effect has often been interpreted as an indication of impaired mitochondrial respiration (Koppenol et al., 2011). However, the relevance of

Significance

B cell receptor (BCR) survival signals are central to pathogenesis of certain DLBCLs. Among transcriptionally defined groups of DLBCL, the "OxPhos" subset displays increased expression of genes involved in mitochondrial oxidative phosphorylation but lacks an intact BCR signaling network, suggesting dependence on alternative survival mechanisms. However, the functional basis of the OxPhos signature has not been defined. Using an integrative approach, we have carefully dissected the patterns of fuel utilization and energy metabolism in DLBCL, with a primary focus on the "OxPhos" subset. We show that fatty acid oxidation and glutathione synthesis are distinct metabolic features of OxPhos-DLBCLs selectively required for their survival. Metabolic signatures may provide important insights into the molecular heterogeneity of DLBCL and reveal rational targets in these lymphomas.

mitochondrial respiration in tumors is varied depending on tumor type, and evidence for an oxidative class of tumors and tumors with dual capacity for glycolytic and oxidative metabolism exists (Marin-Valencia et al., 2012; Moreno-Sánchez et al., 2009). Moreover, the importance of mitochondria in tumor cell survival and proliferation, including utilization of alternative oxidizable substrates such as glutamine and fatty acids, has been increasingly appreciated (Le et al., 2012; Rossignol et al., 2004; Zaugg et al., 2011). The diversity of carbon substrate utilization pathways in tumors is indicative of metabolic heterogeneity that may not only be relevant across different types of cancer but also manifest within a group of tumors that otherwise share a common diagnosis.

Diffuse large B cell lymphomas (DLBCLs) are a genetically heterogeneous group of tumors and the most common non-Hodgkin's lymphomas in adults (Abramson and Shipp, 2005; Lenz and Staudt, 2010). However, the spectrum of fuel utilization pathways and the metabolic fingerprints within DLBCL and other similarly heterogeneous groups of tumors have not been fully elucidated. To date, efforts to capture the molecular heterogeneity of DLBCL have relied on gene expression profiling that has uncovered coordinate signaling and survival paradigms in distinct subsets of DLBCL. In one approach, comparison of the genetic signatures across DLBCLs using genome-wide arrays and multiple clustering algorithms captured tumor-intrinsic distinctions in three separate and reproducible clusters (Monti et al., 2005). Groups of DLBCLs identified by this consensus cluster classification (CCC) scheme are the B cell receptor (BCR)/proliferation cluster (BCR-DLBCL) displaying upregulation of genes encoding BCR signaling components, the OxPhos cluster (OxPhos-DLBCL), which is significantly enriched in genes involved in mitochondrial oxidative phosphorylation (OxPhos), and the host response (HR) tumors largely characterized by a brisk host inflammatory infiltrate (Monti et al., 2005). Another classification framework known as cell of origin (COO) delineated DLBCL subsets that shared components of their transcriptional profiles with normal B cell subtypes, including germinal center B cell (GCB)-like and activated B cell (ABC)-like (Alizadeh et al., 2000), and a third undefined category, designated "type 3" (Wright et al., 2003). CCC and COO classifications capture largely different molecular aspects of DLBCL (Monti et al., 2005).

Unlike tumors that rely on signaling pathways downstream of the BCR, OxPhos-DLBCLs do not display active/functional BCR signaling (Chen et al., 2008). However, the nature of survival pathways in this group of tumors is not known, and beyond the original CCC assignment, the actual functional attributes of the OxPhos molecular signature have not been fully examined. This signature includes multiple subunits of mitochondrial respiratory chain complexes I (NADH dehydrogenase) and V (mitochondrial ATP synthase) that may suggest alterations in mitochondrial energy transduction. However, given the integrative aspect of cellular metabolism and the requirement of both nuclear and mitochondria-encoded genes for proper functioning of the electron transport machinery, the precise metabolic landscape of this molecular subset could not be predicted.

In the present study, we conducted an integrative analysis to dissect the metabolic fingerprints of DLBCL and to delineate subtype-specific differences that may selectively contribute to the growth and survival of DLBCL subsets.

RESULTS

Subtype-Specific Differences in the DLBCL Mitochondrial Proteome

The upregulation of select genes encoding for subunits of electron transport chain (ETC) complexes in OxPhos-DLBCLs predicts potential differences in mitochondrial oxidative metabolism compared with other DLBCL groups. However, as ETC activity is linked to the supply of carbon substrates and reducing equivalents, the OxPhos signature is likely part of a broader spectrum of changes in mitochondrial nutrient metabolism that may shed light on the actual functional attributes of an "OxPhos" program in this DLBCL subset. To search for additional components of this metabolic program, we initially performed two-dimensional differential gel electrophoresis (2D-DIGE) to compare the proteome of mitochondria purified from representative OxPhos- and BCR-DLBCL cell lines Karpas 422 and OCI-Ly1, respectively (Chen et al., 2008). Mitochondrial proteins that were $\geq$2.5 times more abundant in the OxPhos cell line were identified by mass spectrometry (Figure S1A available online). Among 2D-DIGE candidates were subunits of mitochondrial respiratory chain complex I (NADH dehydrogenase), complex II (succinate dehydrogenase, also a tricarboxylic acid [TCA] cycle enzyme), complex V (ATP synthase), subunits of the pyruvate dehydrogenase (PDH) complex and several other TCA cycle enzymes, mitochondrial reactive oxygen species (ROS) detoxification enzyme manganese superoxide dismutase (MnSOD or SOD2), and enzymes involved in mitochondrial β-oxidation of fatty acids and metabolism of ketone bodies and amino acids (Figure S1A).

We next set out to interrogate the mitochondrial protein signature defined by 2D-DIGE in a larger panel of OxPhos- and BCR-DLBCL cell lines. This required an independent proteomics approach amenable to multiplexing—isobaric tags for relative and absolute quantification (iTRAQ) (Figure S1B) (Choe et al., 2007; Ross et al., 2004)—for simultaneous quantitative comparison of multiple unique tryptic peptides per candidate mitochondrial protein across three pairs of OxPhos- and BCR-DLBCL cell lines. This analysis confirmed significant quantitative enrichment of mitochondrial β-oxidation enzymes and multiple subunits of respiratory chain complexes, as well as TCA cycle enzymes and MnSOD in OxPhos-DLBCL mitochondria (Figure 1; Table S1).

Beyond confirming the differential expression of complex I and V components that were in the original OxPhos-DLBCL cluster signature (Monti et al., 2005), the 2D-DIGE and iTRAQ proteomic analyses identified additional components of the OxPhos-DLBCL mitochondrial signature that were not fully captured by the previous RNA profile analysis of total tumors. To examine whether these observations could also be substantiated in primary OxPhos-DLBCLs, we examined tumor biopsies for differences in the abundance of these newly identified components of the mitochondrial signature at both protein and RNA levels. The small en bloc primary DLBCL biopsies precluded isolation of tumor mitochondria; however, iTRAQ-based quantification in a limited number of primary cases that

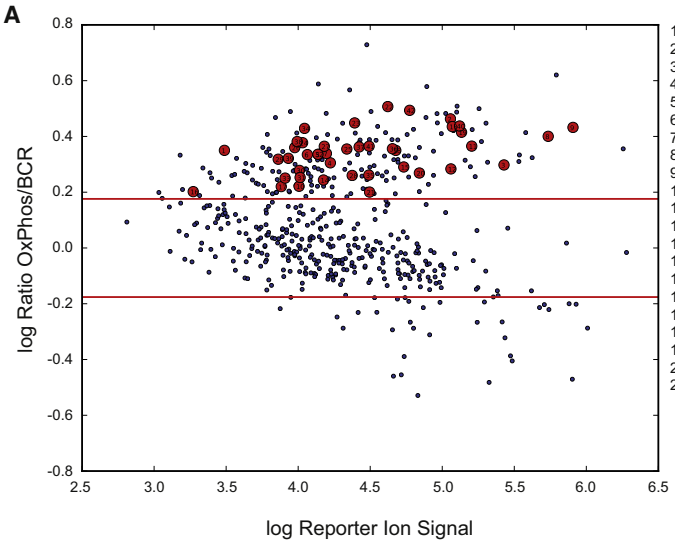

B

TCA Cycle
Pyruvate dehydrogenase (PDH) B
Isocitrate dehydrogenase (IDH) 2 ($NADP^+$)
Isocitrate dehydrogenase (IDH) 3A (NAD^+)
α-Ketoglutarate dehydrogenase (OGDH)
Succinate dehydrogenase (SDH) subunits A and B

Electron Transport and OxPhos Apparatus
Complex I, α subcomplex subunits (NDUFA) 5, 8, 9
Complex I, α subcomplex assembly factor (NDUFAF) 2
Complex I, Fe-S protein (NDUFS) 1, 2, 3
Complex I, flavoprotein (NDUFV) 1, 2, 3
ATP synthase (ATP5) F1 complex subunits
ATP synthase (ATP5) F0 complex subunits

β-Oxidation
Acyl-CoA dehydrogenase (ACAD) VL
Carnitine palmitoyltransferease (CPT) 2
Enoyl-CoA hydratase, short chain (ECHS) 1
Electron-transfer-flavoprotein (ETF) A and B
Hydroxyacyl-CoA dehydrogenase (HADH) A and B

Ketone Body Metabolism
3-oxoacid CoA transferase (OXCT1) 1
Mitochondrial acetoacetyl-CoA thiolase (ACAT1)

Amino Acid and One Carbon Metabolism
Mitochondrial aldehyde dehydrogenase (ALDH) 2
Aldehyde dehydrogenase (ALDH) 1B1
Succinate semialdehyde dehydrogenase (ALDH5A1)
Pyrroline-5-carboxylate synthetase (ALDH18A1)
Mitochondrial serine hydroxymethyltransferase (SHMT2)
Ornithine aminotransferase (OAT)

ROS Detoxification
Manganese Superoxide dismutase (SOD2)

Figure 1. Comparison of Mitochondrial Proteome in OxPhos- and BCR-DLBCLs

(A and B) Multiplex iTRAQ analysis of mitochondria derived from three OxPhos- (Karpas 422, Toledo, and Pfeiffer) and three BCR- (OCI-Ly1, SU-DHL-4, and SU-DHL-6) DLBCL cell lines. Log-log plots of reporter ion abundance ratios versus reporter ion intensities for proteins detected in replicate nanoflow LC-MS/MS analyses are shown in (A). Proteins within the mitochondrial signature that are enriched in OxPhos-DLBCLs are shown as red circles in (A) and grouped per metabolic pathway in (B). Red lines in (A) represent global thresholds based on a ±1.5-fold change between OxPhos and BCR subtypes.
See also Figure S1 and Table S1.

produced protein samples of suitable purity and grade for liquid chromatography/tandem mass spectrometry (LC-MS/MS) indicated increased expression of several TCA cycle and mitochondrial β-oxidation enzymes, as well as MnSOD (Table S1). The RNA abundance for candidate components of the mitochondrial proteome signature was also queried in two extensive primary DLBCL expression profile data sets (Lenz et al., 2008; Monti et al., 2005) with CCC designations (Tables S2 and S3) and found to be significantly higher in primary OxPhos- than in BCR-DLBCLs in both data sets (Figure 2). These observations confirm that the differences in mitochondrial signature identified in DLBCL cell lines translate to primary tumor biopsies.

The functional categories of proteins in the OxPhos-DLBCL mitochondrial signature predict differences in mitochondrial handling of fatty acids and pyruvate, ETC activity, mitochondrial energy production, and ROS content. We next set out to validate each of these predictions.

Mitochondrial Substrate Oxidation in DLBCL Subsets

To assess potential differences in mitochondrial carbon substrate utilization, mitochondrial oxygen consumption rate (OCR) was measured in real time in the absence or presence of exogenously added substrates such as glucose, glutamine, and palmitate, using a panel of 3–4 independent OxPhos and "non-OxPhos" DLBCL cell lines. The non-OxPhos panel included cell lines with known CCC assignment as BCR-DLBCLs (Polo et al., 2007) and COO classification as GCB-, ABC-, or Type 3-DLBCLs (Alizadeh et al., 2000; Wright et al., 2003) (see Supplemental Experimental Procedures). Basal OCR in response to exogenously supplied palmitate was significantly higher in OxPhos-DLBCLs relative to non-OxPhos DLBCL cell lines (no substrate [NS] versus palmitate; Figure 3A). Basal OCR values per individual DLBCL cell line are shown in Figure S2A. The non-OxPhos DLBCLs displayed either no increase in OCR or an increase that was significantly less than that observed in the OxPhos-DLBCLs (Figures 3A and S2A). Notably, the majority of palmitate-stimulated OCR in OxPhos-DLBCLs was sensitive to the mitochondrial ATP synthase inhibitor oligomycin, indicating that mitochondrial fatty acid oxidation (FAO) in this setting is associated with ATP synthesis (Figures 3A and S2A). These observations provide quantitative evidence for increased mitochondrial FAO in OxPhos-DLBCLs. Analysis of other oxidizable substrates showed that none of the DLBCL subsets respire on glucose (NS vs. glucose; Figures 3A and S2A). However, in response to glutamine, all DLBCL subsets exhibited a comparable increase in basal and ATP-associated (oligomycin-inhibitable) OCR (NS versus glutamine; Figures 3A and S2A). Taken together, comparison of the three carbon substrates across and within DLBCL subsets indicates that palmitate is a predominant respiratory fuel in OxPhos-DLBCLs.

A marked increase in palmitate-induced OCR in OxPhos-DLBCL compared with non-OxPhos DLBCL cell lines parallels the absence or presence of functional BCR signaling in these

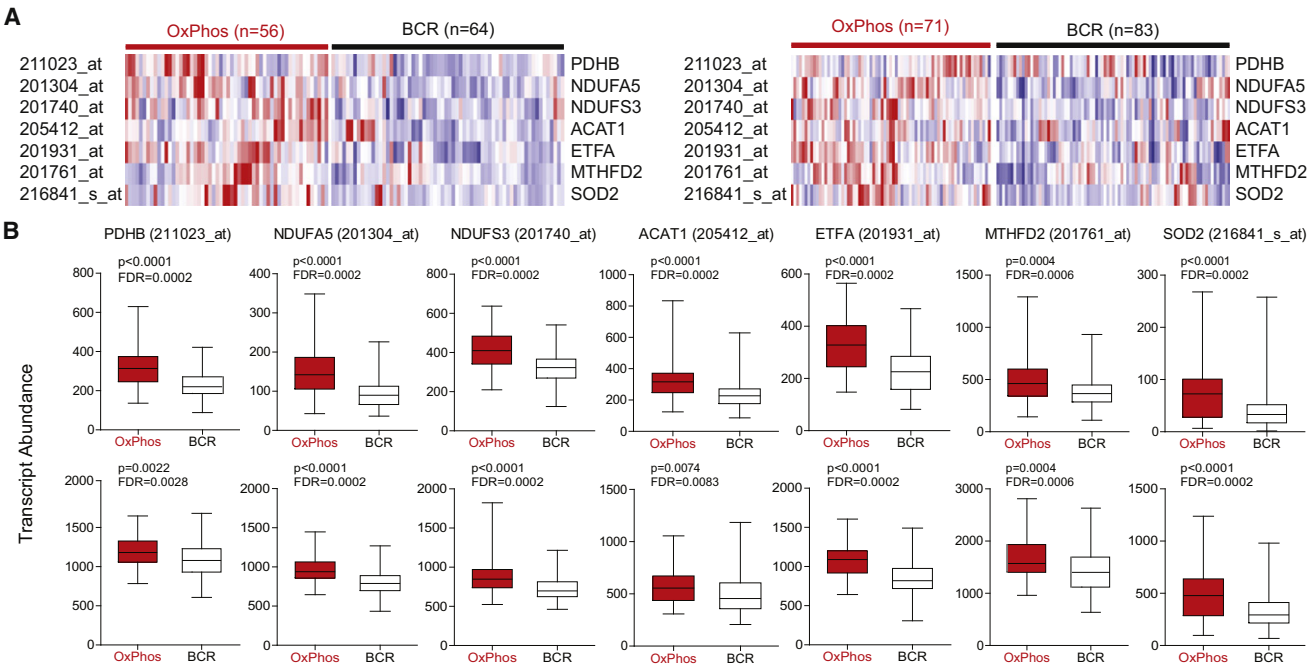

Figure 2. Increased Abundance of Transcripts Encoding Mitochondrial Proteins in Primary DLBCL Tumor Biopsies

(A) Heat map representation of the relative mRNA levels of genes corresponding to the components of the mitochondrial proteome signature using the Monti et al. (left) and Lenz et al. (right) expression array data sets of primary DLBCL cases with OxPhos and BCR consensus cluster assignments.

(B) Transcript abundance (probe intensity) of the indicated genes in primary OxPhos- and BCR-DLBCLs from the Monti et al. (top) and Lenz et al. (bottom) data sets. Differential expression was determined by a two-sided Mann-Whitney test and p values were corrected for multiple hypothesis testing using the false discovery rate (FDR) procedure.

NDUFA5, NADH dehydrogenase (ubiquinone) 1α subcomplex subunit 5; NDUFS3, NADH dehydrogenase (ubiquinone) Fe-S protein 3; ETFA, electron-transfer-flavoprotein A; ACAT1, acetoacetyl-CoA thiolase 1; MTHFD2, methylenetetrahydrofolate dehydrogenase 2; SOD2, manganese superoxide dismutase.

See also Tables S2 and S3.

subsets, respectively (Chen et al., 2008). This prompted examination of a potential reciprocal relationship between active BCR signaling and mitochondrial FAO. Such a scenario would predict that inhibition of BCR signaling in non-OxPhos/BCR DLBCLs may manifest in increased mitochondrial FAO. Indeed, acute interference with BCR signaling using multiple independent shRNAs against SYK, an upstream component of this signaling axis, was associated with significant elevation of basal palmitate-induced OCR (Figure 3B). Notably, OCR measurements were taken after 24 hr treatment with shRNAs, which enabled sufficient depletion of SYK (Figure S2B) without affecting cell viability (data not shown). These observations are suggestive of an underlying metabolic plasticity that governs the pattern of fuel oxidation in DLBCL subsets.

To provide independent and parallel evidence for differential utilization of fatty acids in DLBCL subsets, a targeted ^{13}C isotopomer approach was undertaken. A total of eight cell lines with known designation as OxPhos or BCR were cultured in media containing uniformly labeled ^{13}C-palmitate (U^{13}C-palmitate), and ^{13}C enrichment was assessed in a defined set of intermediates derived from fatty acid metabolism. The complete oxidation of ^{13}C-palmitate by mitochondria yields eight acetyl units that can donate carbons to the TCA cycle in the form of citrate labeled on two carbons ($^{13}C2$-citrate), which can, in turn, lead to the formation of $^{13}C2$-α-ketoglutarate that is in isotopic equilibrium with $^{13}C2$-glutamate (Figure 4A). The relative level of ^{13}C enrichment in both $^{13}C2$-citrate and $^{13}C2$-glutamate was significantly higher in the OxPhos-DLBCL cell lines (Figure 4B). This is consistent with greater entry of palmitate carbons into the TCA cycle.

In addition to oxidative metabolism for energy production, palmitate may have important biosynthetic roles, including direct incorporation into phosphatidyl choline (PC) to yield U^{13}C-Palmitate-PC (Figure 4A). Alternatively, palmitate-derived citrate can be exported from mitochondria and its carbons subsequently incorporated into the head group of PC ($^{13}C2$-acetyl-PC; Figure 4A). In both DLBCL subtypes, direct incorporation of palmitate into PC (U^{13}C-palmitate-PC) was observed. In addition, a larger enrichment of palmitate carbons in $^{13}C2$-acetyl-PC was detected in OxPhos cell lines (Figure 4B).

A preferential increase in palmitate utilization in OxPhos-DLBCLs prompted examination of its effect on proliferation in these cells. Supplementation of serum-free media containing amino acids with palmitate and carnitine led to a modest but significant and selective increase in the proliferation of OxPhos-DLBCLs (Figure 4C). In the absence of palmitate, carnitine, which is required for mitochondrial import of long-chain fatty acids, did not influence proliferation (Figure 4C).

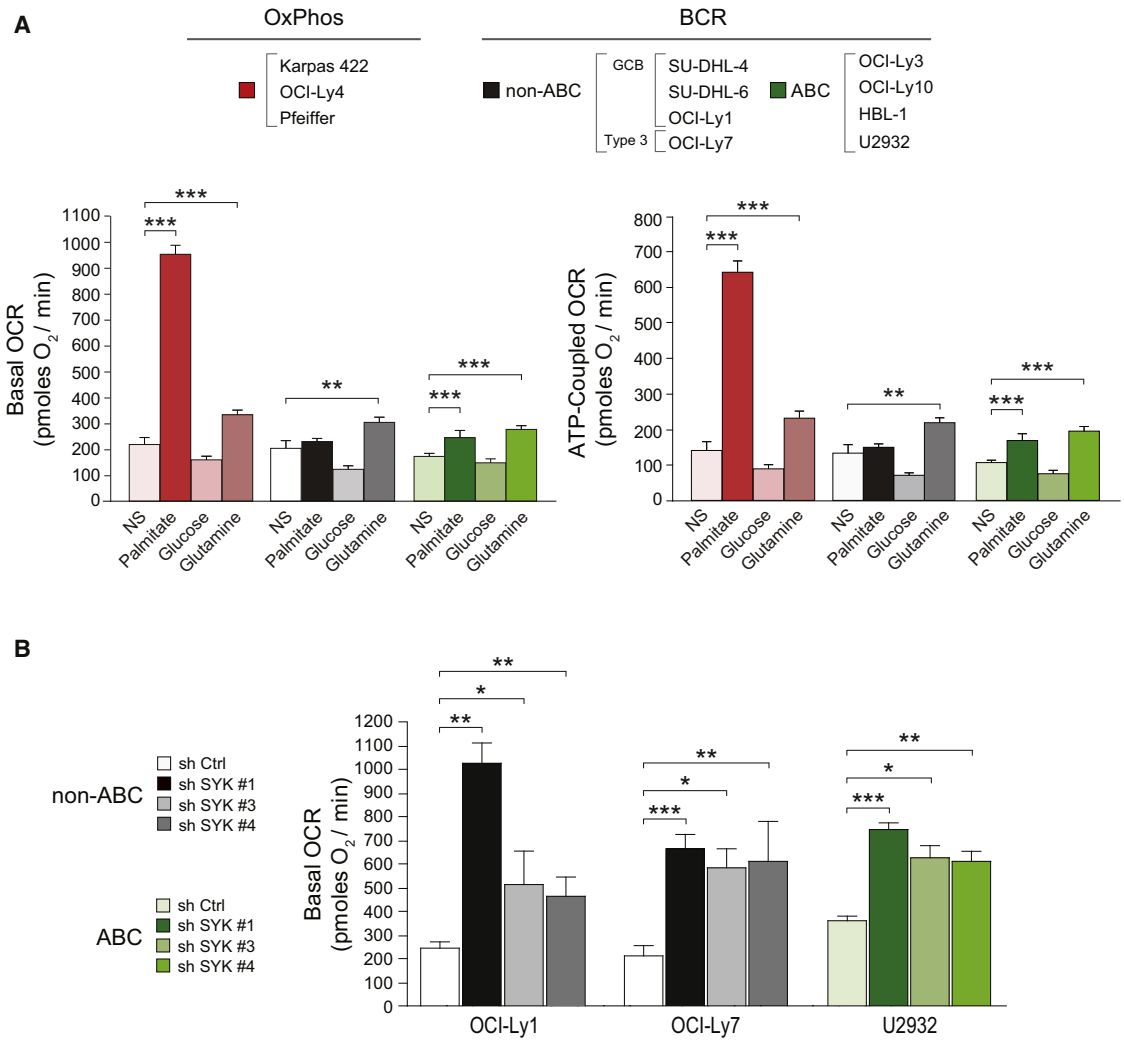

Figure 3. Mitochondrial Carbon Substrate Oxidation in DLBCL Subsets and Its Regulation by BCR Signaling

(A) Basal (left) and ATP-coupled (right) OCR in DLBCL subsets. OCR values shown are the average of all cell lines per DLBCL subtype indicated on top. For each cell line, 7–13 independent OCR measurements were taken. NS, no substrate added exogenously.

(B) Palmitate-stimulated basal OCR in non-OxPhos DLBCL cell lines after acute knockdown of SYK.

Error bars, ±SEM. *$p < 0.05$; **$p < 0.01$; ***$p < 0.001$; two-tailed Student's t test.

See also Figure S2.

To probe the prosurvival benefit of mitochondrial FAO in DLBCL subsets, this program was inhibited using 4-bromocrotonic acid (BrCA), which irreversibly inhibits mitochondrial β-oxidation of both long- and short-chain fatty acids (el-Aleem and Schulz, 1987). Acute treatment of DLBCL cell lines (4 hr) with BrCA interfered with palmitate stimulation of basal OCR in OxPhos-DLBCL cell lines (Figure S3), while longer treatment (24 hr) was selectively toxic to this subset compared with BCR-DLBCLs (Figure 4D). These results suggest that the mitochondrial FAO program provides prosurvival benefits to OxPhos-DLBCLs.

Programmatic Regulation of FAO and Its Relevance to OxPhos-DLBCL Survival

The concomitant increase in the abundance of several mitochondrial FAO enzymes in OxPhos-DLBCLs is consistent, at least in part, with a programmatic increase in the transcriptional regulation of this pathway. These observations warranted systematic interrogation of the primary DLBCL transcript data sets for the prevalence of a defined list of transcriptional regulators of this pathway. Nuclear receptor peroxisome proliferator-activated receptor (*PPAR*) γ transcripts were found to be significantly more abundant in primary OxPhos-DLBCLs in two independent cohorts of DLBCL tumors (Figure S4A). This is consistent with the observation that several enzymes identified in the mitochondrial protein signature of OxPhos-DLBCLs such as ETF, ACAD, and HADH, as well as multiple subunits of mitochondrial respiratory chain complexes I, II, and ATP synthase, are downstream targets of PPARγ (Hsiao et al., 2011). To probe the functional relevance of PPARγ in DLBCL subsets, we tested the effect of its depletion using three independent siRNAs and their corresponding mixture (Figures 5A and S4B).

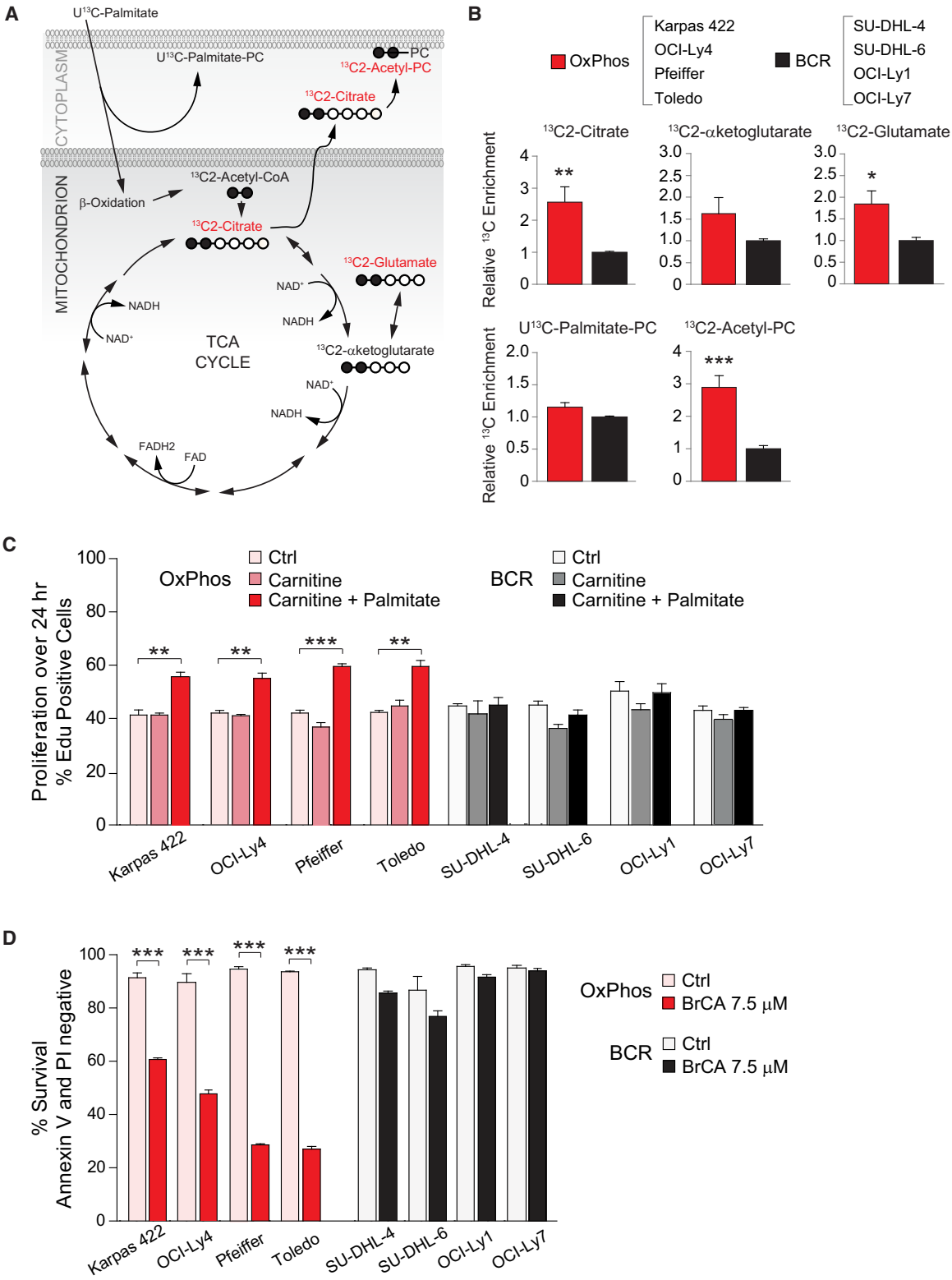

Figure 4. Palmitate Metabolism and Its Effect on DLBCL Proliferation and Survival

(A and B) ^{13}C isotopomer analysis of uniformly labeled palmitate ($U^{13}C$-Palmitate). (A) Schematics depicting the number of carbons labeled (filled circles) in a defined set of metabolites derived from palmitate. Metabolites marked in red are selectively elevated in OxPhos-DLBCL cell lines in (B). (B) ^{13}C enrichment in palmitate-derived metabolites. For each metabolite, cumulative data obtained from all four OxPhos-DLBCL cell lines are shown relative to the mean value of that metabolite in all four BCR-DLBCL cell lines listed on top.

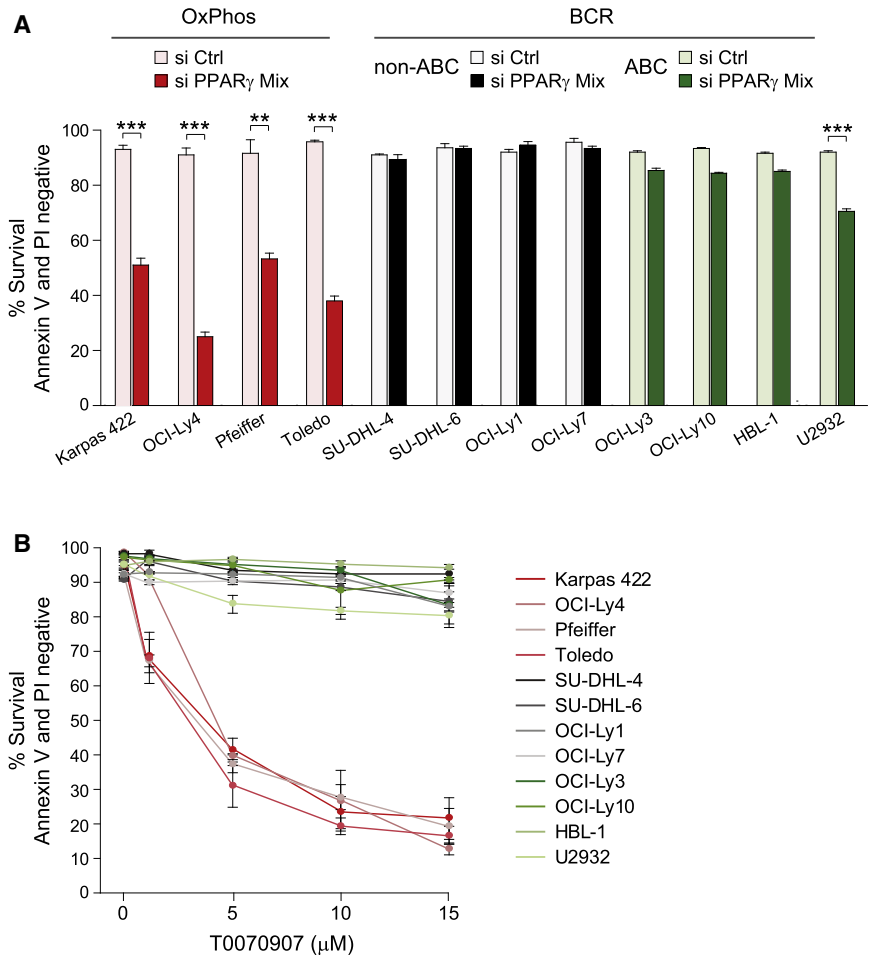

Figure 5. Programmatic Regulation of FAO and Its Relevance to DLBCL Survival

(A) Effect of siRNA-mediated depletion of PPARγ on the survival of DLBCL subsets.

(B) Survival of the indicated DLBCL cell lines cultured in the absence or presence of increasing concentrations of T0070907 for 96 hr.

Error bars, ±SEM. **p < 0.01; ***p < 0.001; two-tailed Student's t test.

See also Figure S4.

The most robust decrease in PPARγ protein levels was achieved using the siRNA mix (Figure S4C) and was accompanied by significant apoptosis in OxPhos-DLBCLs compared with the BCR subset (Figure 5A).

To provide a pharmacologic correlate to these findings, we also tested the effect of two selective PPARγ antagonists T0070907 and GW9662 (Lee et al., 2002; Leesnitzer et al., 2002). Short-term treatment of DLBCL cell lines with these compounds blocked palmitate stimulation of OCR (data not shown). Upon longer incubation periods (96 hr), these compounds proved selectively toxic to OxPhos-DLBCLs (Figures 5B and S4D). The aforementioned genetic and pharmacologic approaches to PPARγ inhibition complement and extend the results shown in Figure 4D that pharmacologic inhibition of mitochondrial β-oxidation program is toxic to OxPhos-DLBCLs and are collectively congruent with the idea that a sustained mitochondrial FAO program may be relevant for the survival of OxPhos-DLBCLs.

Differential Utilization of Glucose-Derived Carbons in DLBCL Subsets

Identification of PDH as a component of the mitochondrial proteome signature in OxPhos-DLBCLs predicts differential mitochondrial handling of pyruvate. Indeed, biochemical analysis of isolated mitochondria derived from a panel of DLBCL cell lines indicated significant increase in PDH enzyme activity in OxPhos-DLBCLs (Figure 6A). Increased PDH activity would further predict diminished availability of glucose-derived pyruvate for lactate synthesis. Biochemical quantification of glucose-derived lactate secreted by OxPhos-DLBCL cell lines compared to non-OxPhos/BCR counterparts indicated that this is indeed the case (Figure 6A). These observations prompted a more detailed examination of the fate of glucose carbons in DLBCL subsets.

Beyond generation of pyruvate, glucose-derived metabolites are central to several biosynthetic pathways (Figure 6B). For example, glucose-6-phosphate can enter the pentose phosphate pathway to yield ribose sugars for nucleic acid synthesis and NADPH generation for lipid synthesis and ROS detoxification (Tennant et al., 2010; Vander Heiden et al., 2009). Dihydroxyacetone phosphate, which is in equilibrium with glyceraldehyde-3-phosphate, is used in glycerol synthesis, providing a necessary backbone for membrane phospholipids. Finally, glucose-derived citrate and aspartate, a surrogate for oxaloacetate (OAA), can be used in lipid and nucleotide synthesis, respectively. To examine differences in the terminal fate of glucose-derived pyruvate and the branch points at which glucose carbons divert to biosynthetic pathways in different DLBCL subsets, we carried out a targeted ^{13}C isotopomer analysis using uniformly labeled ^{13}C-glucose (U^{13}C-glucose).

Glucose uptake was comparable in DLBCL cell lines as evident from the similar levels of remaining U^{13}C-glucose in the

(C) Effect of palmitate supplementation on the proliferation of DLBCL cell lines. Control denotes serum-free media containing all amino acids except L-glutamine.

(D) Survival of DLBCL subsets cultured in the absence or presence of BrCA for 24 hr.

Error bars, ±SEM. *p < 0.05; **p < 0.01; ***p < 0.001; two-tailed Student's t test.

See also Figure S3.

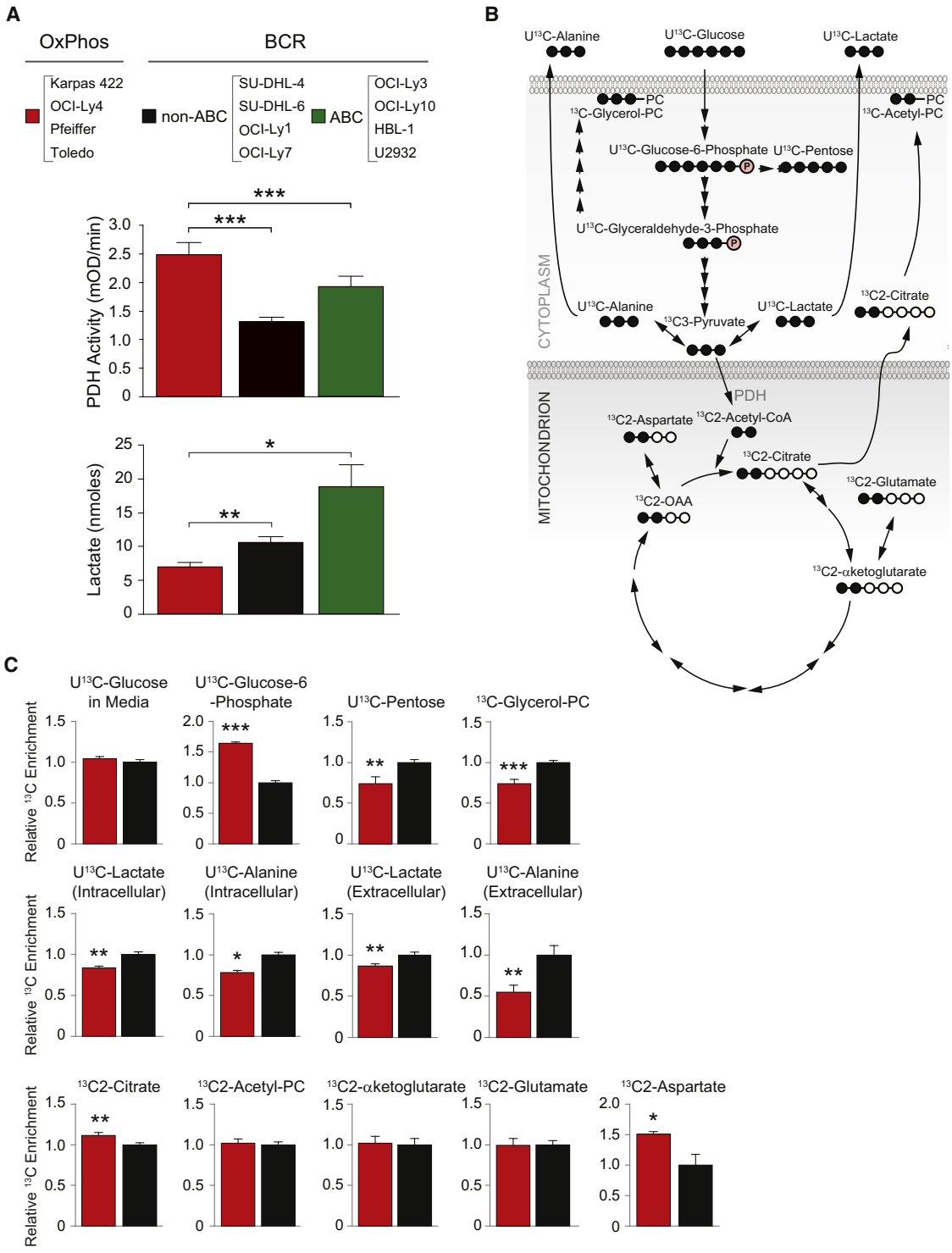

Figure 6. Utilization of Glucose-Derived Carbons in DLBCL Subsets

(A) PDH enzyme activity (middle) and lactate production from glucose (bottom) in DLBCL subsets. Data are cumulative from independent DLBCL cell lines listed on top.

(B and C) ^{13}C isotopomer analysis of uniformly labeled glucose ($U^{13}C$-glucose) (B) Schematics depicting the number of carbons labeled (filled circles) in intermediary metabolites of glucose metabolism. (C) ^{13}C enrichment in glucose-derived metabolites. For each metabolite, cumulative data obtained from all four OxPhos-DLBCL cell lines (Karpas 422, OCI-Ly4, Pfeiffer, and Toledo; red bars) are shown relative to the mean value of that metabolite in all four BCR-DLBCL cell lines (SU-DHL-4, SU-DHL-6, OCI-Ly1, and OCI-Ly7; black bars).

Error bars, ±SEM. *$p < 0.05$; **$p < 0.01$, ***$p < 0.001$; two-tailed Student's t test.

media following 8 hr incubation (Figure 6C). The BCR cell lines displayed a larger contribution of glucose-derived carbons to the synthesis of pentose sugars compared with the OxPhos cell lines ($U^{13}C$-pentose; Figure 6C). This is consistent with reduced levels of $U^{13}C$-glucose-6-phosphate precursor observed in this subset (Figure 6C), provided that the oxidative branch of the pentose phosphate pathway is utilized to derive pentose sugars. In addition, the contribution of glucose carbons to glycerol incorporation into PC was significantly higher in BCR cell lines (^{13}C-glycerol-PC; Figure 6C).

The overall glycolytic capacity was assessed by comparing both intracellular and extracellular (secreted) $U^{13}C$-lactate and $U^{13}C$-alanine (a surrogate for pyruvate). BCR cell lines had significantly higher intracellular and secreted $U^{13}C$-alanine and $U^{13}C$-lactate (Figure 6C). These data are consistent with biochemical evidence that glucose-derived lactate is higher in these cells (Figure 6A), suggesting a higher glycolytic flux.

Glucose-derived pyruvate can enter the TCA cycle through a PDH-catalyzed reaction yielding citrate or through a pyruvate-carboxylase-mediated anaplerotic reaction that generates OAA (Fan et al., 2009). The ratio of PDH and pyruvate carboxylase activities in tumors is variable (DeBerardinis et al., 2007; Fan et al., 2009), suggesting significant diversity and tumor type specificity in the mode of TCA cycle entry of glucose-derived carbons. The PDH reaction can be traced by the pattern of carbon labeling in citrate as $^{13}C2$-citrate. The relative ^{13}C enrichment in this metabolite was significantly higher in OxPhos cell lines (Figure 6C), indicating a greater overall diversion of glucose carbons to the TCA cycle. Elevated PDH-catalyzed formation of $^{13}C2$-citrate in OxPhos-DLBCLs is consistent with increased levels of PDH and enzyme activity in this subset. Among other TCA cycle intermediates measured in this analysis, ^{13}C enrichment in aspartate (surrogate for OAA) was relatively higher in OxPhos compared with BCR cell lines ($^{13}C2$-aspartate; Figure 6C).

Despite elevated PDH activity in OxPhos-DLBCLs and higher enrichment of glucose carbons in the aforementioned TCA cycle intermediates, glucose is not fully oxidized to stimulate mitochondrial OCR in these cells (Figures 3A and S2A). This may be due to greater diversion of glucose-derived TCA intermediates to biosynthetic pathways. Overall, the distinct enrichment patterns of carbons in glucose-derived metabolites indicate relative diminution of lactate production in OxPhos-DLBCL and an attendant increase in the entry of glucose carbons in the TCA cycle via citrate.

Contribution of Mitochondrial Metabolism to Cellular ATP Budget in DLBCL Subsets

The observed differences in utilization of palmitate- and glucose-derived carbons, as well as ATP generation through mitochondrial oxidation of palmitate (ATP-coupled respiration) in DLBCL subsets, warranted comparison of mitochondrial and nonmitochondrial contributions to the cellular energy budget. To this end, the portion of total cellular ATP that is sensitive to inhibition of glycolysis versus mitochondrial metabolism was assessed (Guppy et al., 2002). Compared to BCR-DLBCL, the OxPhos subset derives a significantly higher portion of its total energy (~70%) from mitochondrial oxidative metabolism than from glycolysis (Figure 7A). The higher contribution of mitochondria to total cellular ATP in OxPhos-DLBCLs is concordant with increased expression of mitochondrial ATP synthase (complex V) subunits (Figures 1 and S1A; Table S1) and an elevated rate of mitochondrial ATP synthesis in OxPhos-DLBCL cell lines (Figure 7B). These observations could be potentially explained by differences in mitochondrial content in DLBCL subtypes. However, assessment of the steady-state content of mitochondria in DLBCL cell lines did not reveal any subtype-specific differences (Figure S5A). In addition, mitochondrial SNP copy number analysis in a cohort of primary biopsies with OxPhos or BCR assignments did not reveal any differences (Figure 7C).

Increased contribution of mitochondria to total cellular ATP may reflect not only distinct channeling of carbon substrates in mitochondria but also differential activity or efficiency of mitochondrial ETC complexes. Studies in isolated mitochondria derived from DLBCL cell lines enabled direct assessment of mitochondrial respiration at the organelle level independent of the cytosolic processing of carbon substrates.

Mitochondrial respiratory states were assessed using glutamate/malate and succinate as complex I- and II-linked substrates, respectively (Figures 7D and 7E). When measuring complex II activity, rotenone was included with succinate to inhibit the reverse flow of electrons to complex I. Respiratory rates in the presence of substrate alone (also known as state II respiration) were higher in OxPhos-DLBCL mitochondria (Figure 7F). The addition of ADP, which mimics a state of energy demand driving high rates of respiration (also known as state III respiration) elicited significantly higher OCR in OxPhos-DLBCL mitochondria supplied with either complex I or II substrates (Figure 7F). This increased respiration is used for ATP synthesis and is sensitive to oligomycin. Accordingly, OCR values in the presence of substrate, ADP and oligomycin (state IV respiration) were also significantly higher in OxPhos-DLBCLs compared with BCR-DLBCLs (Figure 7F). These results provide a direct link between the OxPhos signature and an actual quantitative increase in ETC activity in this DLBCL subset. Moreover, independent biochemical measurements of mitochondrial complexes I, II, and IV in immunocapture assays provided corroborative biochemical evidence for significant elevation of these enzyme activities in OxPhos-DLBCLs (Figure S5B). In aggregate, our observations both at the level of intact cells (Figures 3A, 7A, and 7B) and isolated mitochondria (Figures 7F and S5B) demonstrate that the OxPhos signature captures a program of mitochondrial metabolism and energy transduction that is selectively activated in this DLBCL subset.

The Relevance of ROS Content and Glutathione Synthesis in DLBCL Subtypes

Mitochondria are a predominant source of ROS. While ROS signaling is important for a myriad of cellular functions, excessive mitochondrial superoxide can damage mitochondrial DNA, modify proteins and lipids, and inhibit aconitase activity, thus limiting oxidative phosphorylation. Elevated ETC activity in OxPhos-DLBCL, particularly of complex I, predicted increased accumulation of mitochondrial superoxide. However, MnSOD is also concomitantly elevated in this subset (Figures 1, 2, and S1A; Table S1), potentially as a mechanism to counteract increased burden of mitochondrial superoxide. Efficient clearance of ROS would also ensure that oxidative phosphorylation

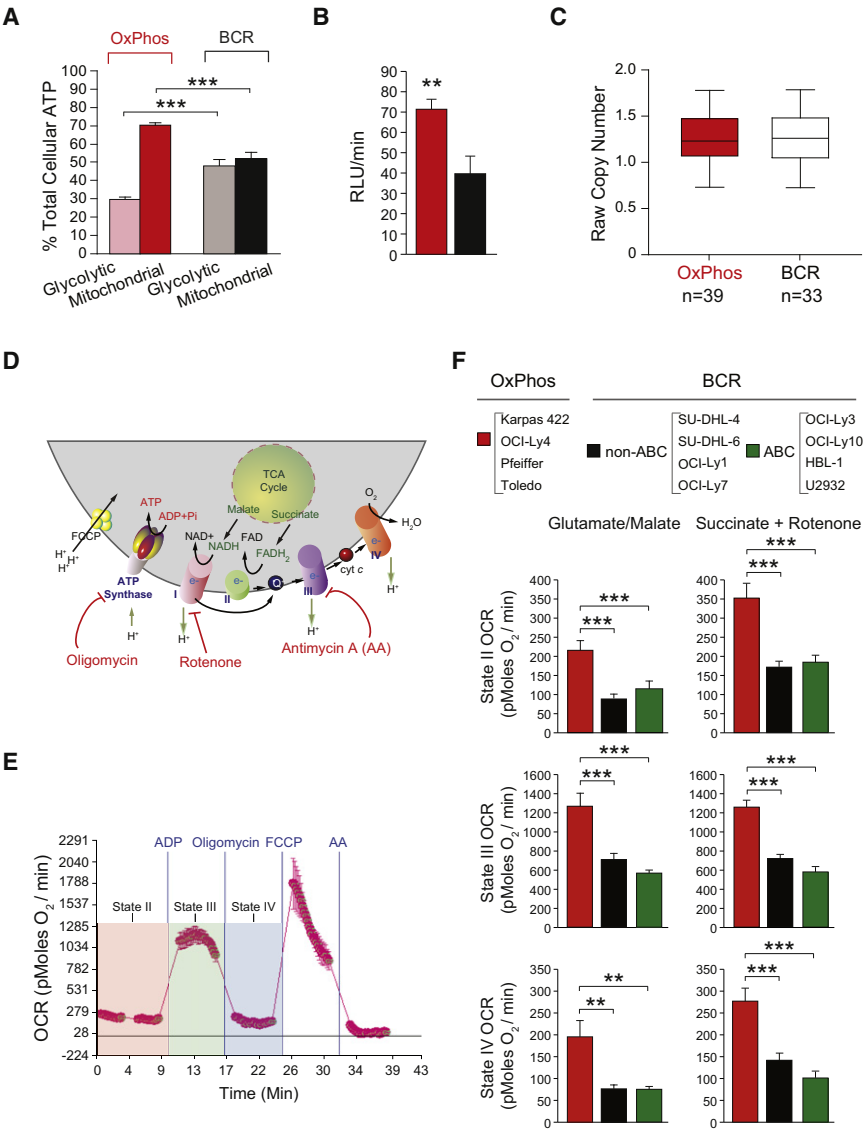

Figure 7. Contribution of Mitochondrial Metabolism to Cellular ATP and Energy Transduction in DLBCL Subsets

(A) Percent contribution of glycolysis and mitochondrial metabolism to total cellular ATP. For each subtype, cumulative data from four OxPhos-DLBCL (Karpas 422, OCI-Ly4, Pfeiffer, and Toledo) and four BCR-DLBCL (SU-DHL-4, SU-DHL-6, OCI-Ly1, and OCI-Ly7) cell lines are shown.

(B) Mitochondrial ATP synthesis rate. Cumulative data from four OxPhos-DLBCL (red bar) and four BCR-DLBCL (black bar) cell lines are shown as in (A).

(C) Average copy number of 110 mitochondrial SNP probes for 39 OxPhos-DLBCL and 33 BCR-DLBCL cases. Differences were tested using a Mann-Whitney U test and found to be nonsignificant.

(D–F) OCR in isolated mitochondria in different respiratory states. (D) Schematics of mitochondrial respiratory complexes and substrates as well as mitochondrial inhibitors used to measure their specific activities. (E) Representative OCR traces in mitochondria isolated from DLBCL cell lines indicating respiratory states examined as described in the Supplemental Experimental Procedures. (F) OCR in isolated mitochondria measured using complex I- or complex II-linked substrates. Data are derived from four cell lines per DLBCL subset listed on top.

Error bars in (A), (B), and (F), ±SEM. $^{**}p < 0.01$; $^{***}p < 0.001$; two-tailed Student's t test.

See also Figure S5.

could remain elevated in OxPhos-DLBCLs. Assessment of mitochondrial superoxide using MitoSOX Red revealed lower steady state levels in OxPhos-DLBCLs (Figure 8A). These observations were further integrated with the total cellular ROS levels using CM-H_2DCFDA, a fluorescent probe that is sensitive to oxidation by peroxyl, alkoxyl, peroxynitrite, $NO2^{\cdot}$, $CO3^{\cdot-}$, and $OH^{\cdot}$ radicals and can thus serve as an indicator of overall oxidative stress. The CM-H_2DCFDA signal intensity was also significantly lower in OxPhos-DLBCLs (Figure 8A). A potential explanation for these observations is increased diversion of peroxide generated from the SOD-catalyzed reaction into the antioxidant glutathione (GSH) system. Consistent with this possibility, GSH levels were significantly higher in OxPhos-DLBCLs (Figure 8A), suggesting increased capacity for ROS detoxification.

Given the quantitative differences in ROS and GSH content in DLBCL cell lines, we hypothesized that the capacity to maintain a large GSH pool may be required for the survival of OxPhos-DLBCLs. To test this possibility, de novo GSH synthesis was inhibited by shRNA-mediated depletion of γ-glutamyl cysteine synthase (GCS), a rate-limiting enzyme that catalyzes the introduction of an amide linkage between the γ-carboxyl group of glutamate and cysteine (Figure 8B). OxPhos-DLBCL cell lines were significantly more sensitive to GCS knockdown compared with the BCR subset (Figures 8C and S6), suggesting that they may be more reliant on GSH for survival.

DISCUSSION

Our integrative analysis using proteomics, mitochondrial respirometry, and metabolomics have unraveled metabolic distinctions in DLBCL subsets. We show that, compared with non-OxPhos/BCR DLBCLs, nutrient and energy metabolism in OxPhos-DLBCL have a significant mitochondrial component, marked by elevated oxidative phosphorylation, increased contribution of mitochondria to total cellular energy budget, greater incorporation of fatty acid- and glucose-derived carbons into the TCA cycle, and increased lipogenesis from these carbon substrates. In comparison, the non-OxPhos DLBCLs have greater glycolytic flux. These studies also provide a clear example of heterogeneity in fuel utilization pathways even within the same disease entity.

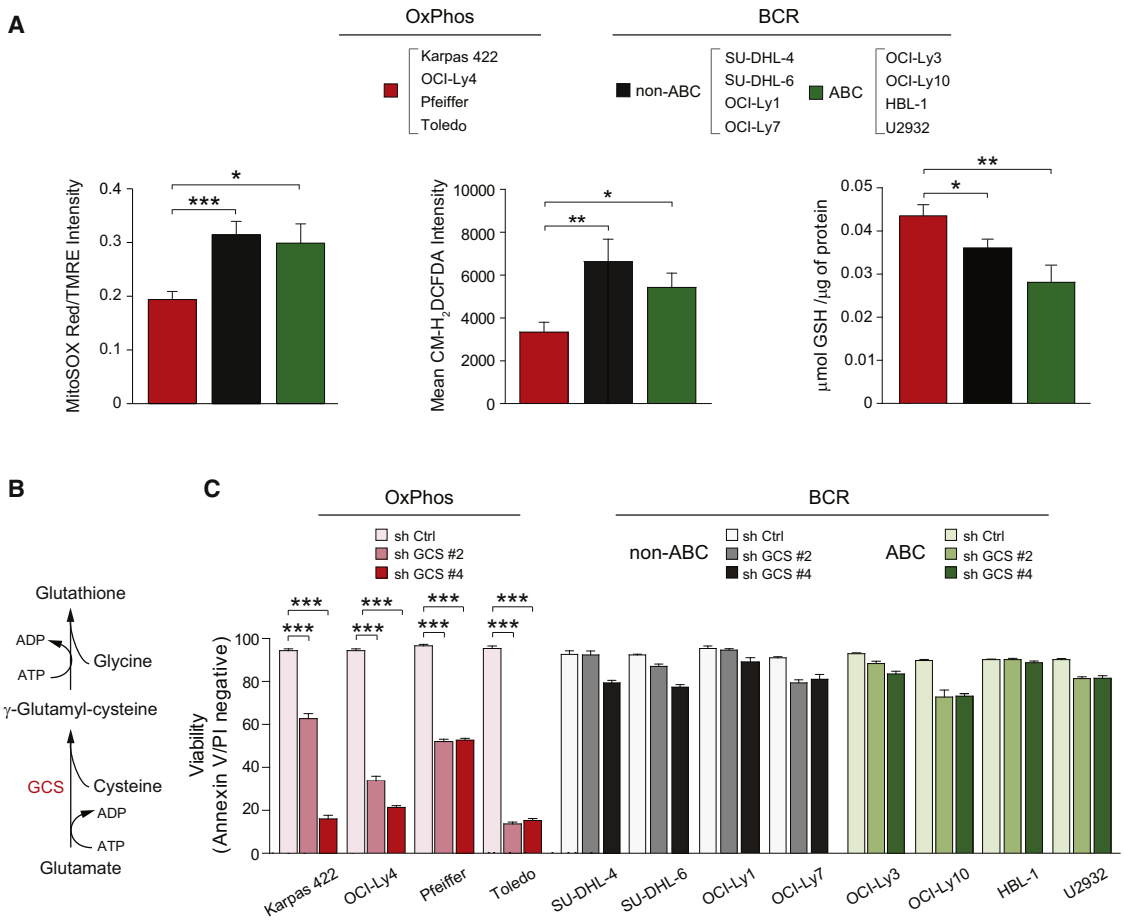

Figure 8. Differential Contribution of ROS Detoxification to Survival of DLBCL Subsets

(A) Mitochondrial superoxide (left), total cellular ROS (middle) and GSH (right) levels in DLBCL subtypes. Data are derived from four cell lines per DLBCL subset listed on top.

(B and C) De novo GSH synthesis pathway (B) and the effect of GCS depletion on DLBCL survival (C). Cell viability was assessed 72 hr after knockdown. GCS, γ-glutamyl cysteine synthase.

Error bars, ±SEM. *$p < 0.05$; **$p < 0.01$, ***$p < 0.001$; two-tailed Student's t test.

See also Figure S6.

The differential utilization of glucose- and fatty-acid-derived carbons in OxPhos versus non-OxPhos DLBCLs appears to parallel the absence or presence of functional BCR signaling, respectively. This is consistent with our observations that acute inhibition of BCR signaling upon SYK depletion is sufficient to enhance palmitate-induced mitochondrial OCR in BCR-DLBCL cell lines. BCR-derived signals are critical for growth and survival of mature B cells as well as multiple B cell lymphomas (Küppers, 2005). These signals also trigger glucose utilization in a PI3K-dependent manner that is marked by an initial increase in lactate production and a subsequent shift to the pentose phosphate pathway during progression to S phase (Doughty et al., 2006). Reduction in glycolytic flux and incorporation of glucose carbons into the pentose pool in OxPhos compared with non-OxPhos DLBCLs is consistent with published observations that OxPhos-DLBCLs do not display the full phosphorylation pattern of signaling intermediates following BCR crosslinking and are insensitive to inhibitors of BCR signaling (Chen et al., 2008).

The common metabolic profile of non-OxPhos DLBCLs is striking, given that these tumors rely on multiple components of BCR signaling (Chen et al., 2008; Compagno et al., 2009; Davis et al., 2010). This may suggest that proliferation and survival mechanisms in these tumors may converge on glycolysis. The clear distinction between the metabolic profiles of OxPhos- and BCR-DLBCLs suggests that the specific pattern of nutrient metabolism in the former may provide an alternative survival program independent of the BCR network. Moreover, the OxPhos metabolic signature may have broader implications for other tumor types that are independent or have lost dependency on the components of BCR signaling.

Several independent approaches to inhibit the mitochondrial FAO program significantly compromised the survival of OxPhos-DLBCL. Within this context, BrCA-mediated inhibition of mitochondrial FAO and pharmacologic or genetic interference with PPARγ were selectively toxic to OxPhos-DLBCL. The relevance of PPARγ in multiple cancer models and the antitumor

effects of its inhibition have been reported (Burton et al., 2008). Increased PPARγ activity has been recently implicated in differentiation and stimulation of antibody production in normal human B-lymphocytes (Garcia-Bates et al., 2009). Whether this is accompanied by increased FAO in normal lymphocytes remains to be determined. Nevertheless, it is possible that the metabolic signature in OxPhos-DLBCL represents pathways relevant to B-lymphocytes that are further modified to fulfill nutrient and energy requirements of these tumors.

Findings in other cancer models have suggested that FAO may serve as an alternative survival pathway that is triggered by glucose deprivation or lack of glucose uptake (Barger and Plas, 2010; Schafer et al., 2009). Moreover, a recent report showed increased FAO in solid tumors contributes to rapamycin resistance (Zaugg et al., 2011). The survival-promoting effect of fatty acid metabolism has also been reported in a leukemia model (Samudio et al., 2010). In this model, increased fatty acid metabolism was decoupled from oxidative phosphorylation, which appears to be distinct from enhanced ATP-coupled OCR in response to palmitate in OxPhos-DLBCL.

Concomitant utilization of palmitate-derived acetyl-CoA for ATP production and citrate synthesis in OxPhos-DLBCL suggests that FAO and fatty acid synthesis may be concurrent pathways in these cells. This may be surprising in light of the inhibitory effect of citrate-derived malonyl-CoA on mitochondrial transport of long-chain fatty acids through carnitine palmitoyltransferase (CPT)1. However, several possibilities may explain these observations. The potency of inhibition by malonyl-CoA differs between the two CPT1 isoforms and is likely further influenced by their relative abundance (McGarry and Brown, 1997). CPT1A is ~80 fold less sensitive to malonyl-CoA than CPT1B and the ratio of CPT1A to 1B expression is higher in OxPhos-DLBCL. The relative abundance of CPT1A and the possibility that malonyl-CoA may be used rapidly prior to its accumulation may explain how mitochondrial FAO could proceed unhindered in these cells. A scenario for rapid utilization of malonyl-CoA is active fatty acid synthesis as would be expected in a proliferating cell. In addition, fatty acid synthesis may serve as a "sink" for excess acetyl CoA/citrate generated due to enhanced FAO and increased entry of acetyl-CoA into the TCA cycle. Concurrent FAO and fatty acid synthesis in other tumors has been observed (Ookhtens and Baker, 1979; Ookhtens et al., 1984). It is also interesting to note that increased FAO in acute myeloid leukemia has been linked to a quiescent pool of tumor-initiating cells (Samudio et al., 2010). The precise molecular basis for concomitant use of fatty acids for ATP production and citrate synthesis in OxPhos-DLBCL awaits future studies.

Parallel activation of an antioxidant defense mechanism with increased mitochondrial FAO in OxPhos-DLBCL is intriguing. A link between FAO and antioxidant capacity has been previously suggested. For example, mitochondrial FAO may serve as a source of NADPH to regenerate GSH (Pike et al., 2011). On the other hand, a reduced cellular redox state may be important for completion of β-oxidation (Korge and Weiss, 2006; Schafer et al., 2009). It is also possible that elevated GSH in OxPhos-DLBCL is secondary to its increased synthesis from glutamate. This is consistent with higher enrichment of fatty-acid-derived glutamate in this subtype. While increased GSH and MnSOD levels are in agreement with lower ROS content, additional mechanisms contributing to ROS handling in OxPhos-DLBCL cannot be excluded.

Our findings provide functional validation of quantifiable metabolic differences associated with transcriptionally defined subsets of DLBCL. These observations also indicate that the OxPhos molecular signature is a bona fide metabolic program that is selectively activated in these lymphomas, providing distinct growth and survival benefits. Detailed fingerprints of the DLBCL metabolome may uncover important insights into the molecular pathogenesis and underlying heterogeneity of these lymphomas as well as additional road maps to subtype-specific therapeutic targets.

EXPERIMENTAL PROCEDURES

Primary DLBCL Biopsies

Protein samples were prepared from frozen biopsy specimens of newly diagnosed, previously untreated primary DLBCLs with >80% tumor involvement according to Institutional Review Board (IRB)-approved protocols from two institutions (Brigham and Women's Hospital and Dana-Farber Cancer Institute). A waiver to obtain informed consent was granted by the IRBs because otherwise discarded tissue was used. The frozen biopsy specimens from which total RNA and high-molecular-weight DNA were extracted for transcript abundance and SNP analysis have been described in a recent study (Monti et al., 2012).

Sample Preparation and Labeling for iTRAQ Analysis

Mitochondria isolated from DLBCL cell lines or Trizol-purified primary biopsy proteins were solubilized in 7.2 M guanidine hydrochloride, 100 mM ammonium bicarbonate. Protein concentration was determined by the Bradford assay (Bio-Rad, Hercules, CA, USA), and equal amounts of protein were reduced with 10 mM dithiothreitol (DTT) for 30 min at 56°C and alkylated with 22.5 mM iodoacetamide for 30 min at room temperature in the dark. DTT was added to a final concentration of 20 mM to quench the remaining iodoacetamide. Proteins were digested overnight with trypsin (1:20) at 37°C after addition of 100 mM ammonium bicarbonate solution to dilute the concentration of guanidine HCl to 1 M. Digests were acidified with 10% trifluoroacetic acid and desalted by C18. Aliquots of peptides were stored at −80°C.

Mitochondria-derived peptides (50 μg) from three OxPhos (Karpas 422, Toledo, and Pfeiffer) and three BCR (OCI-Ly1, SU-DHL-4, and SU-DHL-6) cell lines were solubilized in 100 μl of 30% 500 mM triethylammonium bicarbonate, pH 8.5/70% ethanol, and 1 U of iTRAQ 8-plex reagent was added to each sample (Karpas 422-113, Toledo-114, Pfeiffer-115, OCI-Ly1-117, SU-DHL-4-118, SU-DHL-6-119; note that 116 and 121 reagents were not used). The solution was incubated for 1 hr at room temperature, and the reactions were combined and dried by vacuum centrifugation. Labeled peptides were desalted by C18, dried again by vacuum centrifugation, and stored at −80°C. The same procedure was used to label 100-μg aliquots of primary DLBCL biopsy-derived peptides with iTRAQ 4-plex reagent [biopsy #32 (OxPhos)-114; biopsy #39 (OxPhos)-115; biopsy #42 (BCR)-116)]. iTRAQ-labeled peptide samples were analyzed and data processed as described in Supplemental Experimental Procedures.

Mitochondrial Respirometry

OCR was measured in real time using the XF24 extracellular flux analyzer instrument and the AKOS algorithm v1.5.069 software (Seahorse Bioscience Inc., Chicopee, MA, USA). For whole cell studies, cells were seeded on XF24 V7 plates coated with Cell-Tak (BD Biosciences, Bedford, MA, USA) at 3×10^5 cells/well in 600 μl of sodium bicarbonate-free Roswell Park Memorial Institute (RPMI) medium alone or supplemented with 10 mM glucose, 2 mM glutamine or 0.2 mM palmitate. When palmitate was tested, 0.5 mM carnitine was included in the incubation/equilibration medium to ensure import of bovine serum albumin (BSA)-conjugated palmitate into mitochondria. The plates were spun at 500 rpm (breaks off) and incubated at 37°C for 10 min to ensure cell attachment. Measurements were taken for a total of 60 min, including a 12 min incubation period prior to starting baseline measurements. Within this

assay time, OCR was measured for 3 min periods with 5 intervals between measurements. After baseline measurements, 2.5 μM oligomycin was added in a single 75 μl injection. In all experiments, parallel samples were run in the absence of oligomycin to ensure stable baselines as a quality control parameter for the bioenergetics health of the cells. OCR in isolated mitochondria was determined as detailed in the Supplemental Experimental Procedures.

^{13}C Isotopomer-Based Metabolomics Analysis

Cells (10×10^6) were incubated for 8 hr at 37°C in glutamine-free unbuffered RPMI medium containing 10 mM malate, 0.5 mM carnitine, 10 mM β-hydroxybutyrate, 10% (v/v) fetal bovine serum supplemented with 10 mM glucose, 4 mM glutamine, and 0.2 mM BSA-conjugated palmitate. When tracing glucose or palmitate carbons, the media were supplemented with U-^{13}C-glucose or U-^{13}C-palmitate isotopomers (Cambridge Isotope Laboratories, Andover, MA, USA) to the final concentrations indicated above. Cell pellets and 1 ml aliquots of media were frozen on dry ice and processed for LC-MS/MS and gas chromatography/mass spectrometry (GC/MS) as detailed in the Supplemental Experimental Procedures.

Mitochondrial Copy Number Analysis

The mitochondrial copy number was assessed using the mitochondrial SNP probes within the Affymetrix HD-SNP array 6.0 data from an independent series of primary DLBCL samples (Monti et al., 2012; GEO accession number GSE34171). The presegmentation data processing was performed according to the SNParray 6.0 analytical pipeline described elsewhere (Cancer Genome Atlas Research Network, 2008). Gene expression profiling of the same samples allowed assignment of consensus cluster subtypes (Monti et al., 2012; GEO accession number GSE34171). Subsequently, the average copy number of 110 mitochondrial SNP probes was computed and visualized using a box plot for the 33 BCR and 39 OxPhos samples. Differences were tested using a Mann-Whitney U test (Dawson-Saunders and Trapp, 1994).

Statistics

Unless otherwise indicated, statistical analysis was performed using two-tailed Student's t test, assuming unequal variance. Transcript abundance was visualized with box plots (median, line; 25% and 75% quartile, box; whiskers, minimum to maximum).

SUPPLEMENTAL INFORMATION

Supplemental Information includes six figures, three tables, and Supplemental Experimental Procedures and can be found with this article online at http://dx.doi.org/10.1016/j.ccr.2012.08.014.

ACKNOWLEDGMENTS

We thank Eric Smith for manuscript preparation. We gratefully acknowledge George Rogers, Martin Brand, David Ferrick, Min Wu, and Orian Shirihai for advice on respirometry; Wei Jiang and Frank Cook for assistance with LC-MS/MS and GC/MS; and Georg Lenz and Frank Stegmeier for HBL-1 and U2932 DLBCL cell lines. A.U.K. was supported by the Alexandra Jane Miliotis Fellowship in Pediatric Oncology, the IDEA^2 Program Grant from the Harvard-MIT Division of Health Sciences and Technology, and a Medical Student Research Training Fellowship from the Howard Hughes Medical Institute. E.N. was supported by a postdoctoral fellowship from the Swedish Research Council. This work was supported in part by funding from the Novartis Institutes for Biomedical Research (N.N.D.), National Institutes of Health Grant PO1 CA092625 (M.A.S.), and the German Research Foundation DFG Ch 735/1-1 (B.C.). The authors acknowledge generous support provided through the Dana-Farber Cancer Institute Strategic Research Initiative (to J.A.M.). N.N.D. is a recipient of the Burroughs Welcome Fund Career Award in Biomedical Sciences and a consultant for the Novartis Institutes for Biomedical Research.

Received: June 16, 2011
Revised: June 7, 2012
Accepted: August 20, 2012
Published: October 15, 2012

REFERENCES

Abramson, J.S., and Shipp, M.A. (2005). Advances in the biology and therapy of diffuse large B-cell lymphoma: moving toward a molecularly targeted approach. Blood *106*, 1164–1174.

Alizadeh, A.A., Eisen, M.B., Davis, R.E., Ma, C., Lossos, I.S., Rosenwald, A., Boldrick, J.C., Sabet, H., Tran, T., Yu, X., et al. (2000). Distinct types of diffuse large B-cell lymphoma identified by gene expression profiling. Nature *403*, 503–511.

Barger, J.F., and Plas, D.R. (2010). Balancing biosynthesis and bioenergetics: metabolic programs in oncogenesis. Endocr. Relat. Cancer *17*, R287–R304.

Burton, J.D., Goldenberg, D.M., and Blumenthal, R.D. (2008). Potential of peroxisome proliferator-activated receptor gamma antagonist compounds as therapeutic agents for a wide range of cancer types. PPAR Res. *2008*, 494161.

Cancer Genome Atlas Research Network. (2008). Comprehensive genomic characterization defines human glioblastoma genes and core pathways. Nature *455*, 1061–1068.

Chen, L., Monti, S., Juszczynski, P., Daley, J., Chen, W., Witzig, T.E., Habermann, T.M., Kutok, J.L., and Shipp, M.A. (2008). SYK-dependent tonic B-cell receptor signaling is a rational treatment target in diffuse large B-cell lymphoma. Blood *111*, 2230–2237.

Choe, L., D'Ascenzo, M., Relkin, N.R., Pappin, D., Ross, P., Williamson, B., Guertin, S., Pribil, P., and Lee, K.H. (2007). 8-plex quantitation of changes in cerebrospinal fluid protein expression in subjects undergoing intravenous immunoglobulin treatment for Alzheimer's disease. Proteomics *7*, 3651–3660.

Compagno, M., Lim, W.K., Grunn, A., Nandula, S.V., Brahmachary, M., Shen, Q., Bertoni, F., Ponzoni, M., Scandurra, M., Califano, A., et al. (2009). Mutations of multiple genes cause deregulation of NF-kappaB in diffuse large B-cell lymphoma. Nature *459*, 717–721.

Davis, R.E., Ngo, V.N., Lenz, G., Tolar, P., Young, R.M., Romesser, P.B., Kohlhammer, H., Lamy, L., Zhao, H., Yang, Y., et al. (2010). Chronic active B-cell-receptor signalling in diffuse large B-cell lymphoma. Nature *463*, 88–92.

Dawson-Saunders, B., and Trapp, R. (1994). Basic and Clinical Biostatistics (Norwalk, CT: Appleton & Lange).

DeBerardinis, R.J., Mancuso, A., Daikhin, E., Nissim, I., Yudkoff, M., Wehrli, S., and Thompson, C.B. (2007). Beyond aerobic glycolysis: transformed cells can engage in glutamine metabolism that exceeds the requirement for protein and nucleotide synthesis. Proc. Natl. Acad. Sci. USA *104*, 19345–19350.

DeBerardinis, R.J., Lum, J.J., Hatzivassiliou, G., and Thompson, C.B. (2008). The biology of cancer: metabolic reprogramming fuels cell growth and proliferation. Cell Metab. *7*, 11–20.

Doughty, C.A., Bleiman, B.F., Wagner, D.J., Dufort, F.J., Mataraza, J.M., Roberts, M.F., and Chiles, T.C. (2006). Antigen receptor-mediated changes in glucose metabolism in B lymphocytes: role of phosphatidylinositol 3-kinase signaling in the glycolytic control of growth. Blood *107*, 4458–4465.

el-Aleem, S.A., and Schulz, H. (1987). Evaluation of inhibitors of fatty acid oxidation in rat myocytes. Biochem. Pharmacol. *36*, 4307–4312.

Fan, T.W., Lane, A.N., Higashi, R.M., Farag, M.A., Gao, H., Bousamra, M., and Miller, D.M. (2009). Altered regulation of metabolic pathways in human lung cancer discerned by (13)C stable isotope-resolved metabolomics (SIRM). Mol. Cancer *8*, 41.

Garcia-Bates, T.M., Baglole, C.J., Bernard, M.P., Murant, T.I., Simpson-Haidaris, P.J., and Phipps, R.P. (2009). Peroxisome proliferator-activated receptor gamma ligands enhance human B cell antibody production and differentiation. J. Immunol. *183*, 6903–6912.

Guppy, M., Leedman, P., Zu, X., and Russell, V. (2002). Contribution by different fuels and metabolic pathways to the total ATP turnover of proliferating MCF-7 breast cancer cells. Biochem. J. *364*, 309–315.

Hsiao, G., Chapman, J., Ofrecio, J.M., Wilkes, J., Resnik, J.L., Thapar, D., Subramaniam, S., and Sears, D.D. (2011). Multi-tissue, selective PPARγ modulation of insulin sensitivity and metabolic pathways in obese rats. Am. J. Physiol. Endocrinol. Metab. *300*, E164–E174.

Koppenol, W.H., Bounds, P.L., and Dang, C.V. (2011). Otto Warburg's contributions to current concepts of cancer metabolism. Nat. Rev. Cancer *11*, 325–337.

Korge, P., and Weiss, J.N. (2006). Redox regulation of endogenous substrate oxidation by cardiac mitochondria. Am. J. Physiol. Heart Circ. Physiol. *291*, H1436–H1445.

Küppers, R. (2005). Mechanisms of B-cell lymphoma pathogenesis. Nat. Rev. Cancer *5*, 251–262.

Le, A., Lane, A.N., Hamaker, M., Bose, S., Gouw, A., Barbi, J., Tsukamoto, T., Rojas, C.J., Slusher, B.S., Zhang, H., et al. (2012). Glucose-independent glutamine metabolism via TCA cycling for proliferation and survival in B cells. Cell Metab. *15*, 110–121.

Lee, G., Elwood, F., McNally, J., Weiszmann, J., Lindstrom, M., Amaral, K., Nakamura, M., Miao, S., Cao, P., Learned, R.M., et al. (2002). T0070907, a selective ligand for peroxisome proliferator-activated receptor gamma, functions as an antagonist of biochemical and cellular activities. J. Biol. Chem. *277*, 19649–19657.

Leesnitzer, L.M., Parks, D.J., Bledsoe, R.K., Cobb, J.E., Collins, J.L., Consler, T.G., Davis, R.G., Hull-Ryde, E.A., Lenhard, J.M., Patel, L., et al. (2002). Functional consequences of cysteine modification in the ligand binding sites of peroxisome proliferator activated receptors by GW9662. Biochemistry *41*, 6640–6650.

Lenz, G., and Staudt, L.M. (2010). Aggressive lymphomas. N. Engl. J. Med. *362*, 1417–1429.

Lenz, G., Wright, G., Dave, S.S., Xiao, W., Powell, J., Zhao, H., Xu, W., Tan, B., Goldschmidt, N., Iqbal, J., et al; Lymphoma/Leukemia Molecular Profiling Project. (2008). Stromal gene signatures in large-B-cell lymphomas. N. Engl. J. Med. *359*, 2313–2323.

Marin-Valencia, I., Yang, C., Mashimo, T., Cho, S., Baek, H., Yang, X.L., Rajagopalan, K.N., Maddie, M., Vemireddy, V., Zhao, Z., et al. (2012). Analysis of tumor metabolism reveals mitochondrial glucose oxidation in genetically diverse human glioblastomas in the mouse brain in vivo. Cell Metab. *15*, 827–837.

McGarry, J.D., and Brown, N.F. (1997). The mitochondrial carnitine palmitoyltransferase system. From concept to molecular analysis. Eur. J. Biochem. *244*, 1–14.

Monti, S., Chapuy, B., Takeyama, K., Rodig, S., Hao, Y., Yeda, K., Inguilizian, H., Mermel, C., Curie, T., Dogan, A., et al. (2012). Integrative analysis reveals an outcome-associated and targetable pattern of p53 and cell cycle deregulation in diffuse large B-cell lymphoma. Cancer Cell *22*, 359–372.

Monti, S., Savage, K.J., Kutok, J.L., Feuerhake, F., Kurtin, P., Mihm, M., Wu, B., Pasqualucci, L., Neuberg, D., Aguiar, R.C., et al. (2005). Molecular profiling of diffuse large B-cell lymphoma identifies robust subtypes including one characterized by host inflammatory response. Blood *105*, 1851–1861.

Moreno-Sánchez, R., Rodríguez-Enríquez, S., Saavedra, E., Marín-Hernández, A., and Gallardo-Pérez, J.C. (2009). The bioenergetics of cancer: is glycolysis the main ATP supplier in all tumor cells? Biofactors *35*, 209–225.

Morrish, F., Neretti, N., Sedivy, J.M., and Hockenbery, D.M. (2008). The oncogene c-Myc coordinates regulation of metabolic networks to enable rapid cell cycle entry. Cell Cycle *7*, 1054–1066.

Ookhtens, M., and Baker, N. (1979). Fatty acid oxidation to H2O by Ehrlich ascites carcinoma in mice. Cancer Res. *39*, 973–980.

Ookhtens, M., Kannan, R., Lyon, I., and Baker, N. (1984). Liver and adipose tissue contributions to newly formed fatty acids in an ascites tumor. Am. J. Physiol. *247*, R146–R153.

Pike, L.S., Smift, A.L., Croteau, N.J., Ferrick, D.A., and Wu, M. (2011). Inhibition of fatty acid oxidation by etomoxir impairs NADPH production and increases reactive oxygen species resulting in ATP depletion and cell death in human glioblastoma cells. Biochim. Biophys. Acta *1807*, 726–734.

Polo, J.M., Juszczynski, P., Monti, S., Cerchietti, L., Ye, K., Greally, J.M., Shipp, M., and Melnick, A. (2007). Transcriptional signature with differential expression of BCL6 target genes accurately identifies BCL6-dependent diffuse large B cell lymphomas. Proc. Natl. Acad. Sci. USA *104*, 3207–3212.

Ross, P.L., Huang, Y.N., Marchese, J.N., Williamson, B., Parker, K., Hattan, S., Khainovski, N., Pillai, S., Dey, S., Daniels, S., et al. (2004). Multiplexed protein quantitation in Saccharomyces cerevisiae using amine-reactive isobaric tagging reagents. Mol. Cell. Proteomics *3*, 1154–1169.

Rossignol, R., Gilkerson, R., Aggeler, R., Yamagata, K., Remington, S.J., and Capaldi, R.A. (2004). Energy substrate modulates mitochondrial structure and oxidative capacity in cancer cells. Cancer Res. *64*, 985–993.

Samudio, I., Harmancey, R., Fiegl, M., Kantarjian, H., Konopleva, M., Korchin, B., Kaluarachchi, K., Bornmann, W., Duvvuri, S., Taegtmeyer, H., and Andreeff, M. (2010). Pharmacologic inhibition of fatty acid oxidation sensitizes human leukemia cells to apoptosis induction. J. Clin. Invest. *120*, 142–156.

Schafer, Z.T., Grassian, A.R., Song, L., Jiang, Z., Gerhart-Hines, Z., Irie, H.Y., Gao, S., Puigserver, P., and Brugge, J.S. (2009). Antioxidant and oncogene rescue of metabolic defects caused by loss of matrix attachment. Nature *461*, 109–113.

Tennant, D.A., Durán, R.V., and Gottlieb, E. (2010). Targeting metabolic transformation for cancer therapy. Nat. Rev. Cancer *10*, 267–277.

Vander Heiden, M.G., Cantley, L.C., and Thompson, C.B. (2009). Understanding the Warburg effect: the metabolic requirements of cell proliferation. Science *324*, 1029–1033.

Wright, G., Tan, B., Rosenwald, A., Hurt, E.H., Wiestner, A., and Staudt, L.M. (2003). A gene expression-based method to diagnose clinically distinct subgroups of diffuse large B cell lymphoma. Proc. Natl. Acad. Sci. USA *100*, 9991–9996.

Yuneva, M.O., Fan, T.W., Allen, T.D., Higashi, R.M., Ferraris, D.V., Tsukamoto, T., Matés, J.M., Alonso, F.J., Wang, C., Seo, Y., et al. (2012). The metabolic profile of tumors depends on both the responsible genetic lesion and tissue type. Cell Metab. *15*, 157–170.

Zaugg, K., Yao, Y., Reilly, P.T., Kannan, K., Kiarash, R., Mason, J., Huang, P., Sawyer, S.K., Fuerth, B., Faubert, B., et al. (2011). Carnitine palmitoyltransferase 1C promotes cell survival and tumor growth under conditions of metabolic stress. Genes Dev. *25*, 1041–1051.

Cancer Cell, Volume *22*

Supplemental Information

Metabolic Signatures Uncover Distinct Targets in Molecular Subsets of Diffuse Large B Cell Lymphoma

Pilar Caro, Amar U. Kishan, Erik Norberg, Illana A. Stanley, Bjoern Chapuy, Scott B. Ficarro, Klaudia Polak, Daniel Tondera, John Gounarides, Hong Yin, Feng Zhou, Michael R. Green, Linfeng Chen, Stefano Monti, Jarrod A. Marto, Margaret A. Shipp, and Nika N. Danial

Inventory of Supplemental Information

SUPPLEMENTAL DATA

A

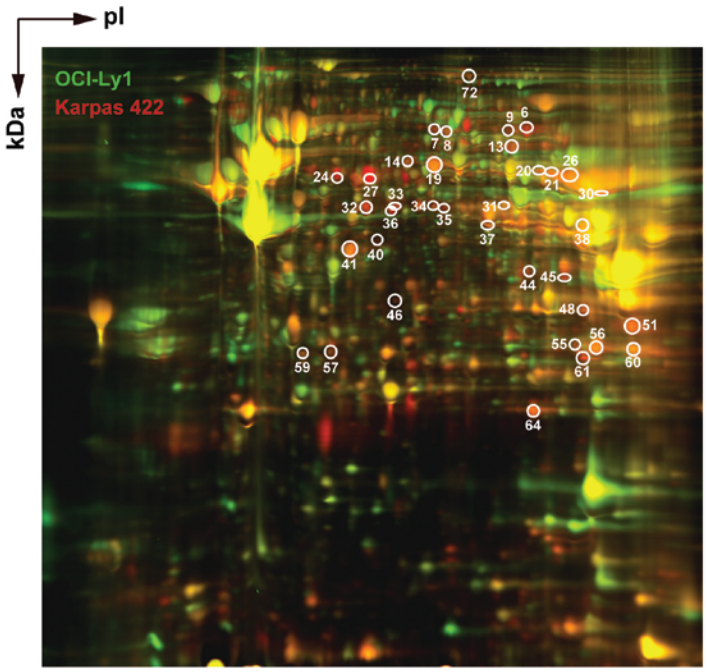

Spot ID and Gene Symbol	Peptide Count	Protein Name	Metabolic Pathway
6- PCK2	31	Phosphoenolpyruvate carboxykinase (mitochondrial)	TCA cycle
7- SDHA	20	Succinate dehydrogenase subunit A	TCA cycle
8- SDHA	21	Succinate dehydrogenase subunit A	TCA cycle
9- PCK2	32	Phosphoenolpyruvate carboxykinase 2 (mitochondrial)	TCA cycle
13- AIF	20	Apoptosis Inducing Factor (Aif)	OXPHOS
14- OXCT1	16	3-oxoacid CoA transferase 1 precursor	Ketone body metabolism
19- OXCT1	16	3-oxoacid CoA transferase 1 precursor	Ketone body metabolism
20- ALDH5A1	12	Aldehyde dehydrogenase 5A1, succinate semialdehyde dehydrogenase	Amino acid metabolism
21- ATP5A	18	ATP synthase F1 complex α subunit	OXPHOS
24- ALDH2	21	Mitochondrial aldehyde dehydrogenase	Amino acid and alcohol metabolism
26- ATP5A	19	ATP synthase F1 complex α subunit	OXPHOS
27- ALDH2	23	Mitochondrial aldehyde dehydrogenase	Amino acid and alcohol metabolism
30- SHMT2	21	Mitochondrial serine hydroxymethyltransferase	Amino acid metabolism
31- PDH	13	Pyruvate dehydrogenase	TCA cycle
32- LC25A24	20	Mitochondrial carrier protein (ANT1)	ADP, ATP transport
33- LC25A24	20	Mitochondrial carrier protein (ANT1)	ADP, ATP transport
34- NDUFS2	20	Mitochondrial carrier portein (ANT1)	ADP, ATP transport
35- NDUFS2	22	NADH dehydrogenase (ubiquinone) Fe-S protein 2	Electron transport
36- OAT	27	Ornithine aminotransferase precursor	Amino acid metabolism
37- MCAD	21	Medium chain acyl- CoA dehydrogenase	Mitochondrial β-oxidation
38- ACAT1	14	Mitochondrial acetoacetyl-CoA thiolase (T2)	Ketone body metabolism
40- OXCT1	11	3-oxoacid CoA transferase 1 precursor	Ketone body metabolism
41- IDH3A	17	Isocitrate dehydrogenase 3 (NAD+) α precursor	TCA cycle
44- TOM40	11	Translocase of outer mitochondrial membrane	Mitochondrial protein import
45- MTHFD2	12	Methylenetetrahydrofolate dehydrogenase	One carbon metabolism
46- NDUFA1	14	Complex I α subcomplex assembly factor 1	Electron transport
48- HADH	8	Hydroxyacyl-CoA dehydrogenase	Mitochondrial β-oxidation
51- VDAC3	13	Voltage-dependent anion channel 3	Translocation of adenine nucleotides
55- AK2	10	Adenylate kinase 2	Transfer of phosphate between ATP and AMP
56- ETF	11	Electron-transfer-flavoprotein	Mitochondrial β-oxidation
57- ECHS1	6	Enoyl-CoA hydratase short Chain 1	Mitochondrial β-oxidation
59- NDUFS3	17	Complex I Fe-S protein 3	Electron transport
60- SDHB	13	Succinate dehydrogenase subunit B	TCA cycle
61- AK2	11	Adenylate kinase 2	Transfer of phosphate between ATP and AMP
64- SOD2	12	Superoxide dismutase [Mn], mitochondrial	ROS detoxification
72- OGDH	40	Oxoglutarate (α-ketoglutarate) dehydrogenase	TCA cycle

B

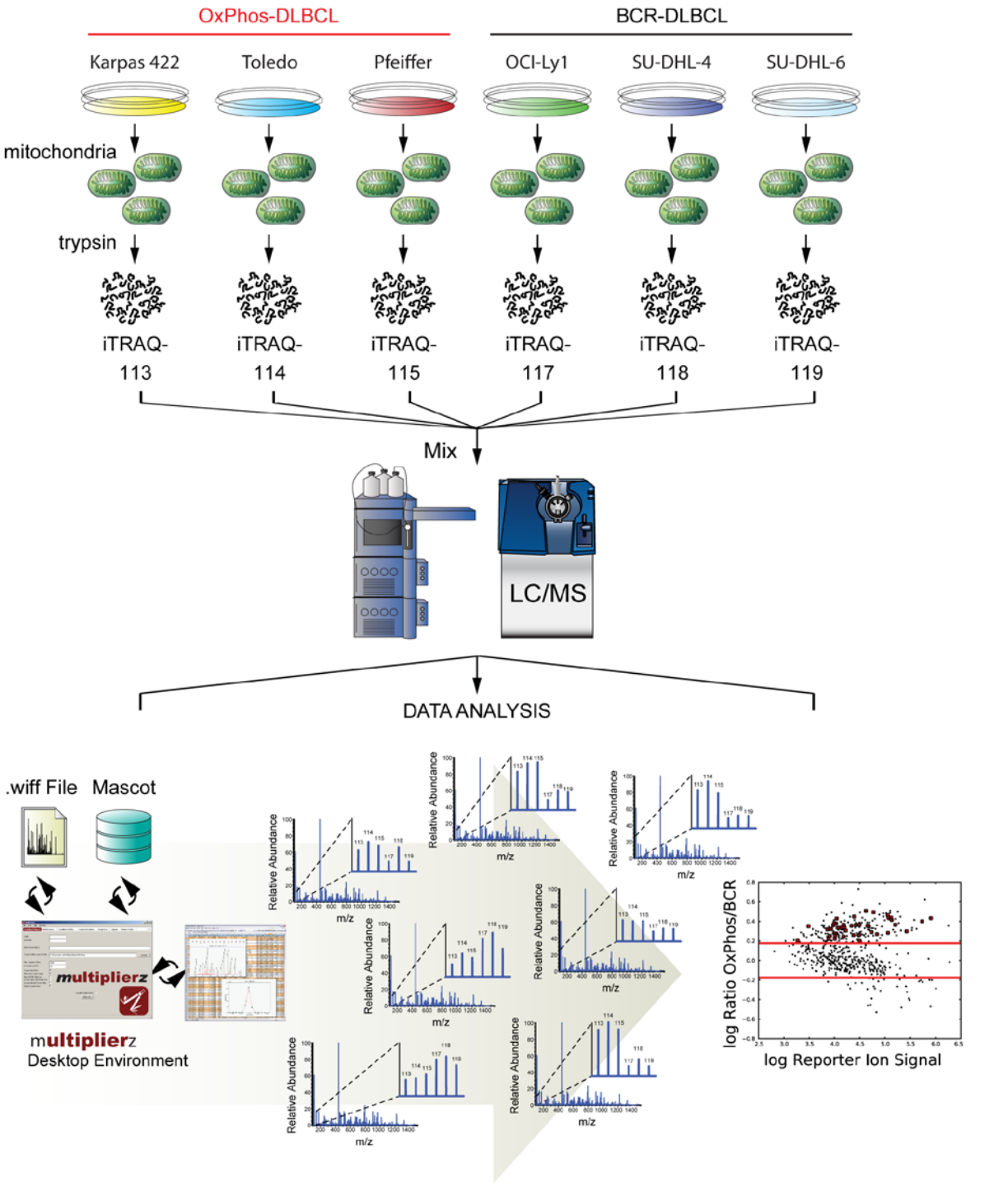

Measure iTRAQ reporter ion intensities for multiple unique tryptic peptides across genes/proteins of interest

Derive abundance ratios by summing reporters for all peptides mapping to unique genes across replicates

Figure S1, related to Figure 1. Mitochondrial protein signature in OxPhos-DLBCL. (A) 2D-DIGE comparison of mitochondria isolated from Karpas 422 (OxPhos) and OCI-Ly1 (BCR) DLBCL cell lines. Equivalent amounts of mitochondrial protein lysates (prepared as detailed in the supplemental experimental procedures) from OCI-Ly1 and Karpas 422 cell lines were labeled with Cy3 and Cy5 DIGE fluors, respectively, mixed and resolved on a 2D analytical gel (Applied Biomics, inc., Hayward, CA) (left panel). Image scans were carried out and the differential protein expressions (Cy5/Cy3) were determined using DeCyder software (version 6.5, GE-Healthcare). Proteins that were ≥ 2.5 fold more abundant in OxPhos-DLBCL were picked by Ettan Spot Picker (GE-Healthcare) and subjected to in-gel trypsin digestion, peptide extraction, desalting, and MALDI-TOF/TOF mass spectrometry (Applied Biosystems). Protein species in red display higher abundance in the OxPhos-DLBCL cell line Karpas 422. pI, iso-electric point. Identity and metabolic function of up-regulated mitochondrial proteins in Karpas 422 are shown in the right panel. (B) Schematics of analytical work flow for multiplex iTRAQ analysis of mitochondria isolated from DLBCL cell lines. Mitochondria isolated from the indicated DLBCL cell lines were subjected to tryptic digestion and iTRAQ labeling and analyzed by LC-MS/MS as described in experimental procedures. MS files were searched using Mascot version 2.2.1 against a forward-reversed human (38190 forward entries) NCBI refseq database with an appended cRAP database of 752 entries. An excel spreadsheet containing the mascot search results was generated using Multiplierz version 0.8.3. Abundance ratios for the protein candidates within the mitochondrial protein signature (defined in Figure S1A) were derived by summing reporters for all peptides mapping to unique genes across replicates. Only genes represented by 2 or more unique peptides are reported (Table S1). See experimental procedures for additional details on data collection and analysis.

A

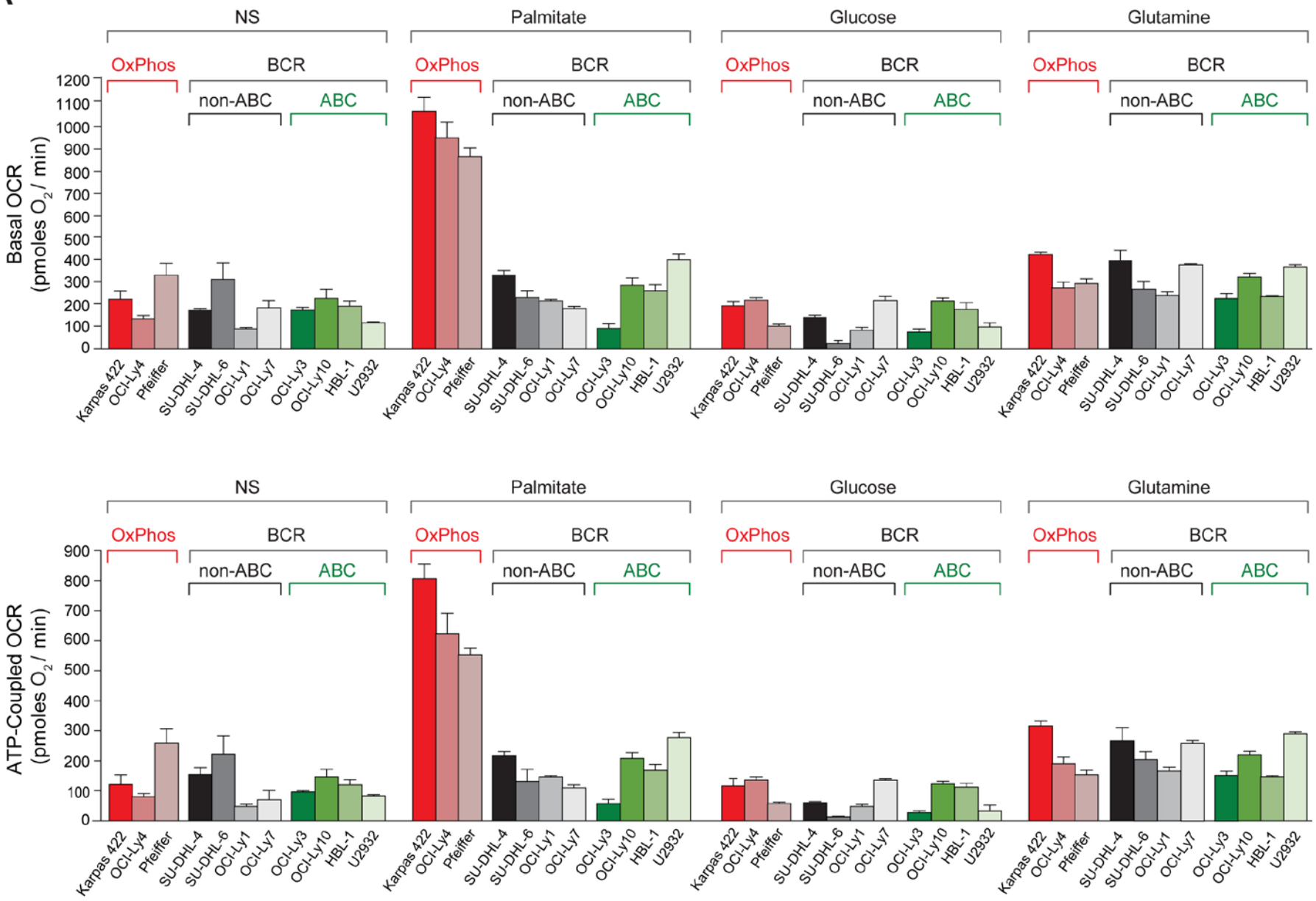
NS
Palmitate
Glucose
Glutamine
OxPhos
BCR
non-ABC
ABC
Basal OCR (pmoles O2 / min)
ATP-Coupled OCR (pmoles O2 / min)
Karpas 422
OCI-Ly4
Pfeiffer
SU-DHL-4
SU-DHL-6
OCI-Ly1
OCI-Ly7
OCI-Ly3
OCI-Ly10
HBL-1
U2932

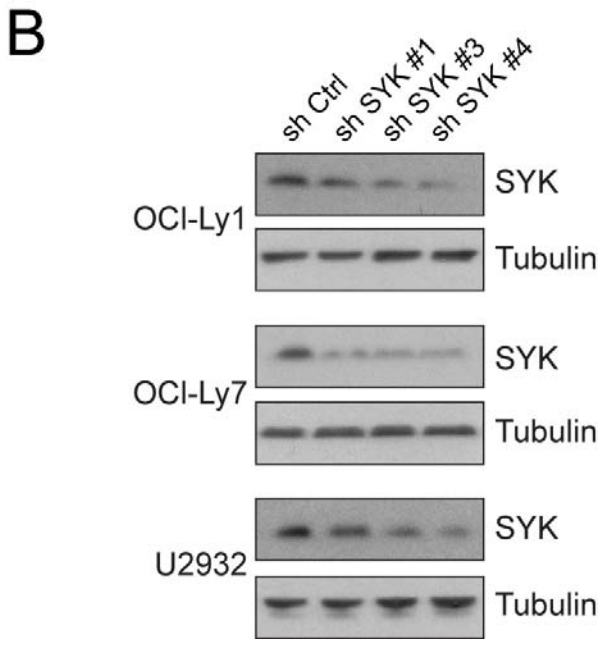

Figure S2, related to Figure 3. Mitochondrial carbon substrate oxidation in DLBCL subsets. (A) Basal (top) and ATP-coupled (bottom) OCR in individual DLBCL cell lines. For each cell line, the mean of 7-13 independent respirometry experiments (independent days and independent plates and cartridges for the XF24 flux analyzer instrument) is shown. NS denotes no substrate added exogenously. See Supplemental Experimental Procedures for cell line assignments per CCC and COO classification schemes. Error bars, ± SEM. (B) Efficiency of shRNA-mediated SYK depletion. SYK protein levels 24 hr after cells were infected with the indicated lentiviruses. This time point was also used to analyze the effect of palmitate on basal OCR in these same cell lines (main Figure 3B).

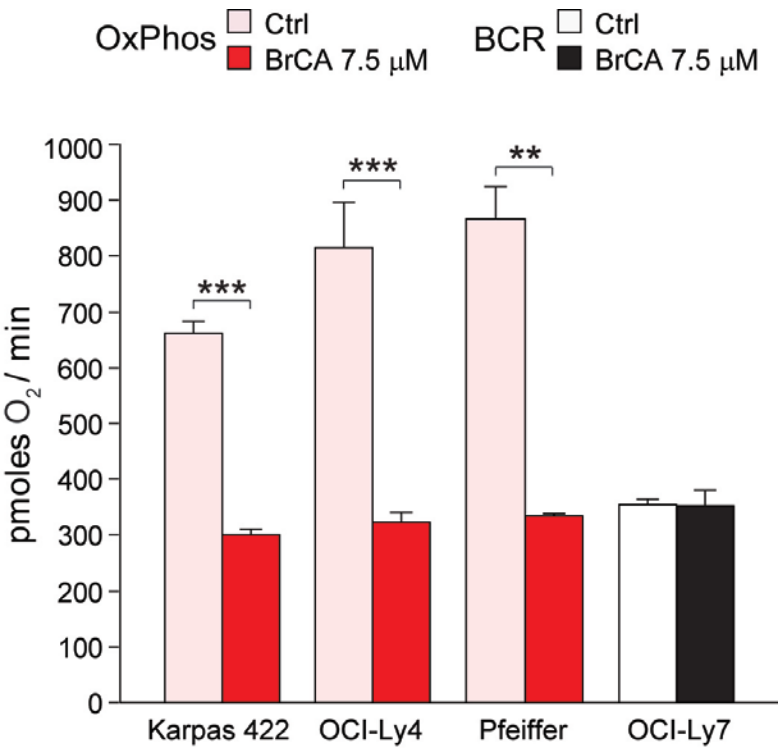

Figure S3, related to Figure 4. Effect of acute bromocrotonic acid treatment on palmitate-stimulated basal OCR in DLBCL cell lines. The indicated cell lines were treated with 7.5 μM of bromocrotonic acid (BrCA) for 4 hr and basal OCR was measured in response to palmitate as the only exogenously added substrate. Error bars, ± SEM. **p<0.01; ***p < 0.001; two-tailed Student's *t*-test.

A

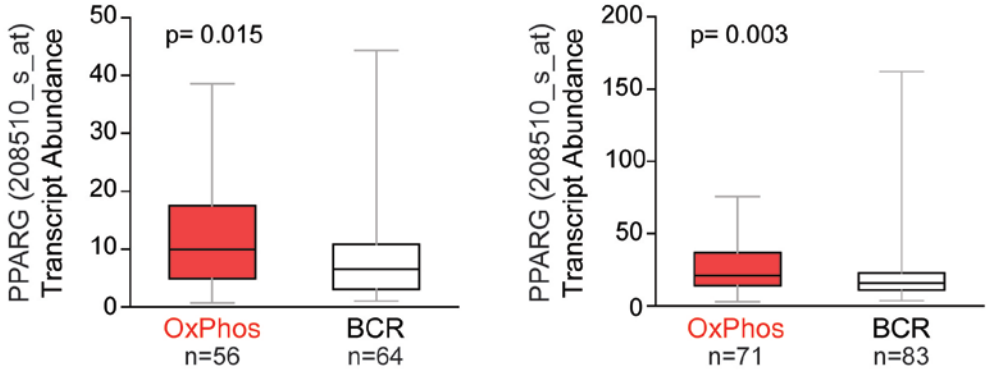
PPARG (208510_s_at) Transcript Abundance
p= 0.015
OxPhos
n=56
BCR
n=64
PPARG (208510_s_at) Transcript Abundance
p= 0.003
OxPhos
n=71
BCR
n=83

B

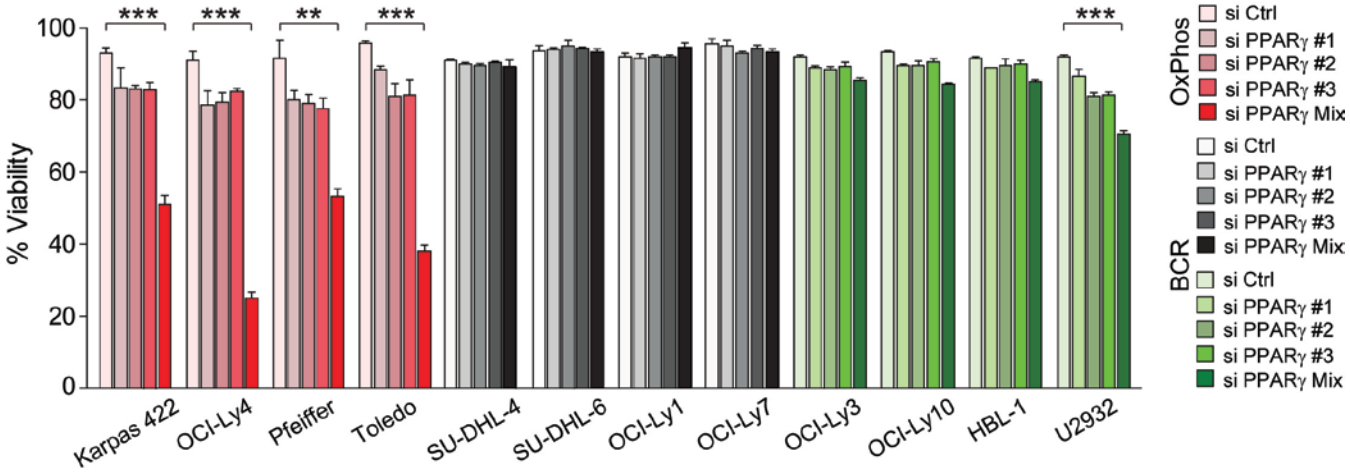
% Viability
Karpas 422
OCI-Ly4
Pfeiffer
Toledo
SU-DHL-4
SU-DHL-6
OCI-Ly1
OCI-Ly7
OCI-Ly3
OCI-Ly10
HBL-1
U2932
OxPhos
BCR
si Ctrl
si PPARγ #1
si PPARγ #2
si PPARγ #3
si PPARγ Mix

C

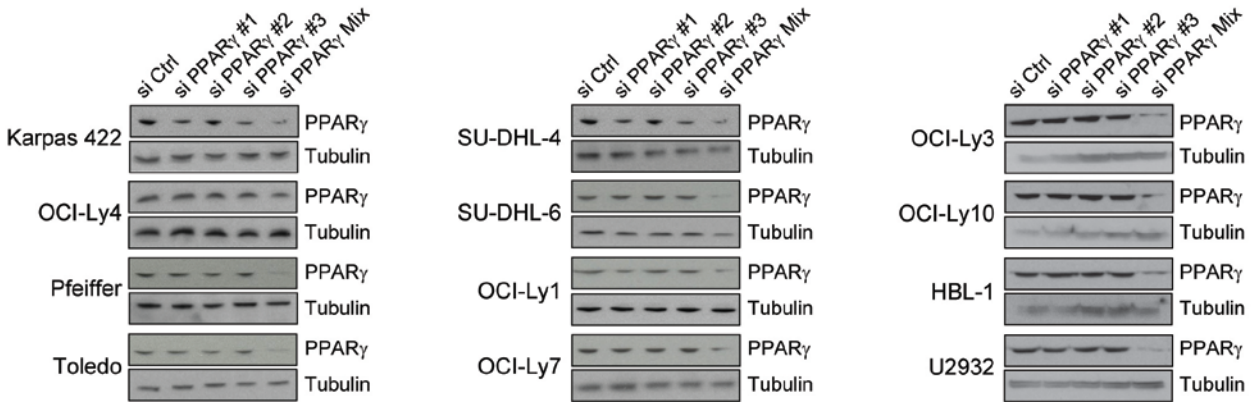
si Ctrl
si PPARγ #1
si PPARγ #2
si PPARγ #3
si PPARγ Mix
Karpas 422
OCI-Ly4
Pfeiffer
Toledo
SU-DHL-4
SU-DHL-6
OCI-Ly1
OCI-Ly7
OCI-Ly3
OCI-Ly10
HBL-1
U2932
PPARγ
Tubulin

D

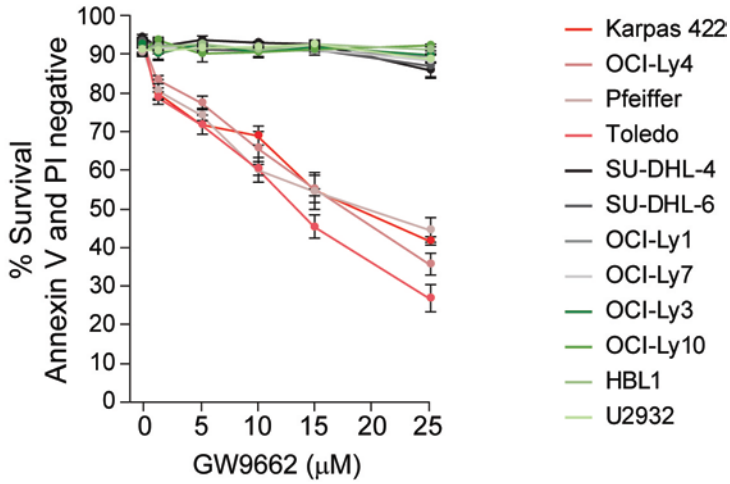

Figure S4, related to Figure 5. Relevance of PPARγ to the survival of OxPhos-DLBCLs. (A) Increased transcript abundance of PPARγ in the Monti *et al*. (left) and Lenz *et al*. (right) data sets of primary DLBCL cases with OxPhos and BCR consensus cluster assignments. See also Table S2. Differential expression was determined by a two-sided Mann Whitney test and p values were corrected for multiple hypothesis testing using the false discovery rate (FDR) procedure. (B) Viability of DLBCL cell lines after 72 hr treatment with individual or a mixture of 3 independent siRNAs against PPARγ. Error bars, ± SEM. **p < 0.01; ***p < 0.001; two-tailed Student's *t*-test. (C) Western blot analysis of PPARγ levels in DLBCL cell lines subjected to siRNA as in (B), showing best knockdown efficiency was achieved with the mixture of independent siRNAs. (D) Survival of the indicated DLBCL cell lines cultured in the absence or presence of increasing concentrations of the PPARγ antagonist GW9662 for 96 hr. Error bars, ± SEM.

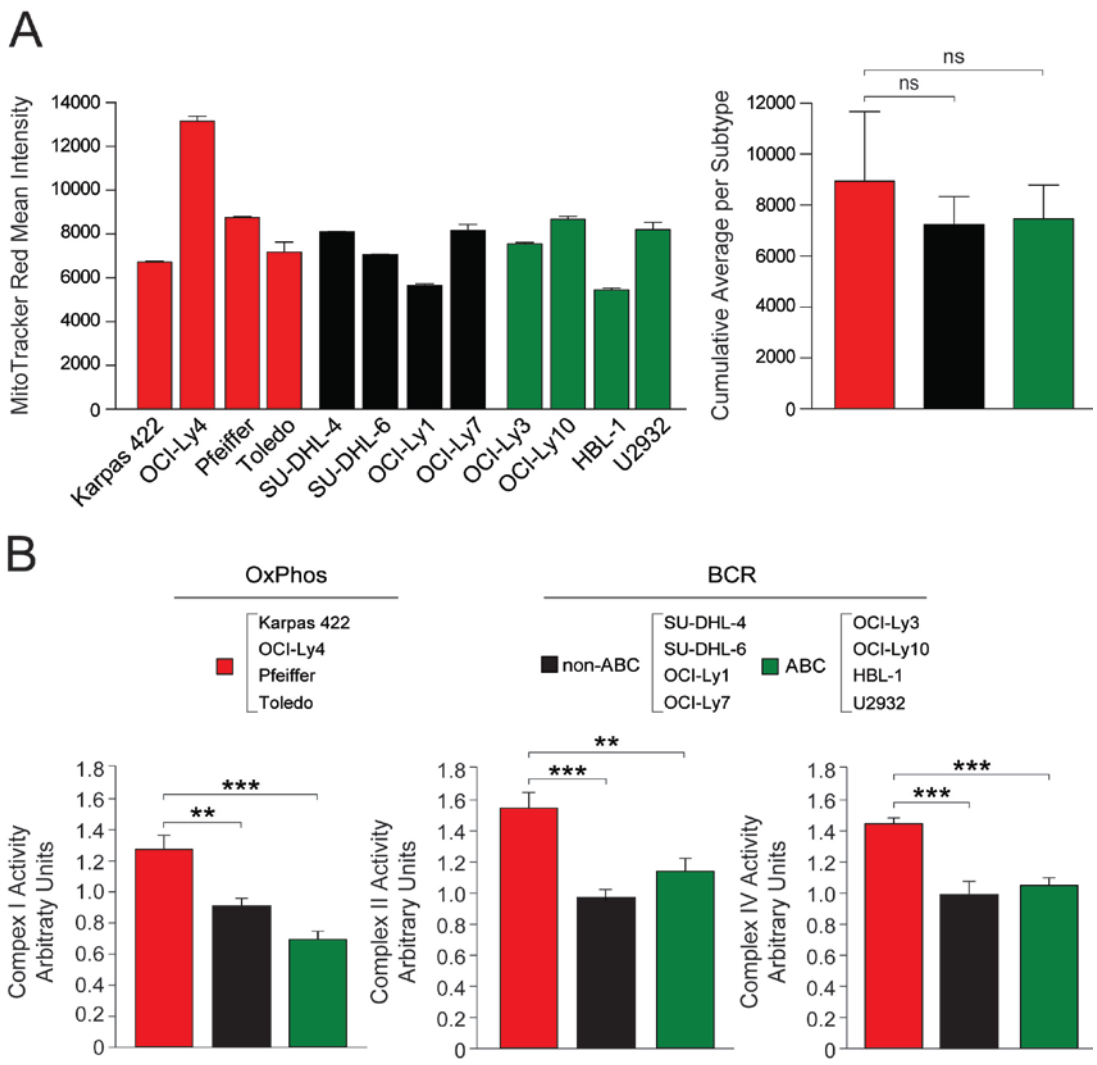

Figure S5, related to Figure 7. Mitochondrial content and electron transport chain activity in DLBCL cell lines. (A) Mitochondrial content in DLBCL cell lines measured using MitoTracker Red. Values per individual cell line (left) and cumulative average per subtype (right) are shown. (B) Activity of respiratory chain complexes I (NADH dehydrogenase), II (succinate dehydrogenase) and IV (cytochrome *c* oxidase) in mitochondria isolated from 4 independent DLBCL cell lines per subtype (listed on top) using capture-based enzyme activity assays (MitoScience, Eugene, OR). The amount of mitochondria used was 100 μg for complexes I and IV and 10 μg for complex II activity measurements. Data show cumulative values from 4-8 independent experiments with 3-4 replicates for each cell line. Error bars, ± SEM. ns, non-significant; **p < 0.01; *** p < 0.001; two-tailed Student's *t*-test.

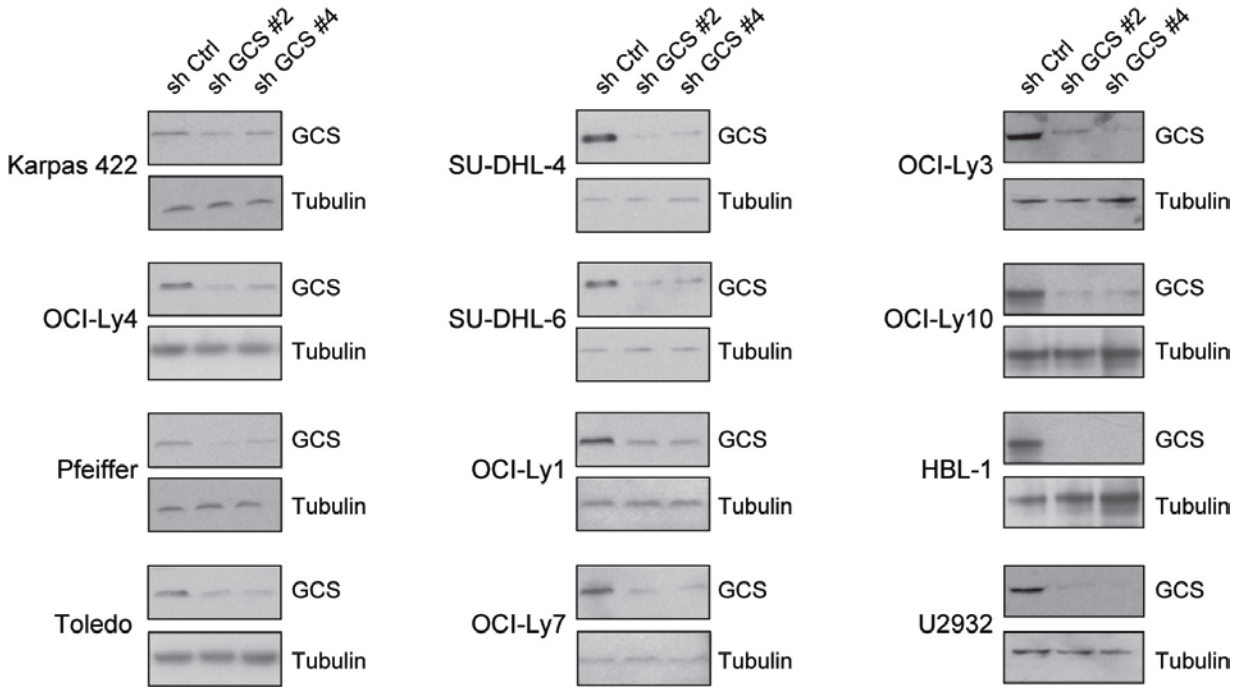

Figure S6, related to Figure 8. Efficiency of shRNA-mediated GCS depletion. GCS protein levels 72 hr after the indicated DLBCL cell lines were infected with lentiviruses bearing shRNA against GCS or control viruses**.**

SUPPLEMENTAL EXPERIMENTAL PROCEDURES

Classification of DLBCL primary tumor biopsies and cell lines based on RNA profiles. Primary DLBCL samples were assigned to consensus clusters using their transcriptional profiles and an ensemble classification scheme previously described (Polo et al., 2007). In particular, 13 independent classifiers were trained on the original 141-sample series of DLBCL samples (Monti et al., 2005) and applied to the 233 R-CHOP treated samples to be classified (Lenz et al., 2008). Class membership was determined by majority voting, and samples with fewer than 10 of 13 classifiers in agreement were left unassigned. The number and identity of the predictive features (probe sets) used to build each of the 13 classifiers were determined by leave-one-out cross-validation in the training set.

Cell Line	Classification	
	CC	COO
SU-DHL-4	BCR	GCB
SU-DHL-6	BCR	GCB
OCI-Ly1	BCR	GCB
OCI-Ly7	BCR	Type 3
Karpas 422	OxPhos	GCB
OCI-Ly4	OxPhos	Type 3
Pfeiffer	OxPhos	Type 3
Toledo	OxPhos	Type 3
OCI-Ly3	BCR	ABC
OCI-Ly10	BCR	ABC
HBL-1*	N/A	ABC
U2932*	N/A	ABC

DLBCL cell lines used in this study (Karpas 422, OCI-Ly4, Pfeiffer, Toledo, SU-DHL-4, SU-DHL-6, OCI-Ly1, OCI-Ly7, OCI-Ly3, OCI-Ly10, HBL-1 and U2932) have been previously described (Chen et al., 2008; Davis et al., 2010). The consensus cluster (CC) assignments of these DLBCL cell lines have been previously defined (Chen et al., 2008; Polo et al., 2007). The cell-of-origin (COO) designation was determined based on the previously described linear predictive score (LPS) method (Wright et al., 2003), built upon the 23 (of 27) COO probe sets represented in the microarray. Cell lines were assigned to the GCB class if their classification probability was greater than 0.9, to the ABC class if their probability was less than 0.1, and to Type 3 otherwise. See also the cell line table to the left for summary of class designations per CC and COO classification schemes.

* Intact BCR signaling and dependency BCR-mediated survival signaling has been confirmed for the HBL-1 and U2932 “ABC-type” DLBCL cell lines [(Kloo et al., 2011) and M. Shipp, personal communication].

Cell Culture, inhibitor treatment and viability assays. All cell lines were grown in RPMI supplemented with 10% fetal bovine serum, 2 mM glutamine, and 1% penicillin/streptomycin with the following exceptions. HBL1 cells were cultured in the above medium containing 1% sodium pyruvate. OCI-Ly3 and OCI-Ly10 cells were cultured in IMDM supplemented with 20% fetal bovine serum or human serum AB (Gemini, West Sacramento, CA), respectively. For inhibitor studies, $2.5x10^6$ cells were treated with 4-bromocrotic acid (International Lab, San Francisco, CA) at 7.5 μM for 24 hr or with T007090 (Sigma) at 1, 5, 10, 15 μM for 96 hr at 37°C. Cell viability was measured using the Annexin V:FITC Apoptosis Detection Kit (BD Bioscience) followed by flow cytometry.

Mitochondria isolation. Cells were resuspended in mitochondria isolation buffer (MIB; 200 mM mannitol, 70 mM sucrose; 1 mM EGTA; 10 mM HEPES, pH 7.4) containing protease inhibitors, homogenized with 20 strokes of a teflon-glass homogenizer, and resuspended in MIB. The nuclei and cell debris were removed by two consecutive centrifugations at 1000 g for 10 min and the supernatant containing crude mitochondria was centrifuged twice at 9000 g for 20 min. The resultant pellet contained mitochondria-enriched heavy membrane (HM) fraction. For respirometry and enzyme activity assays, the HM fraction was resuspended in MIB. For 2D-DIGE analysis (Figure S1), the pellet containing the HM fraction was resuspended in MOPS/mannitol buffer (5 mM MOPS, 300 mM mannitol, pH 7.5), carefully overlaid onto a 30/70 % percoll/MOPS/mannitol gradient and centrifuged at 20,000 g for 40 min. Purified mitochondria were collected at the interface between the 30 and 70% percoll gradients, resuspended and washed three times in MOPS/mannitol buffer containing 1mg/ml defatted BSA.

LC-MS/MS analysis of iTRAQ-labeled samples. Approximately 500 ng of iTRAQ labeled peptides were analyzed in duplicate by nano LC-MS/MS (Ficarro et al., 2009) using a NanoAcquity UPLC system (Waters, Milford, MA) and quadrupole time-of-flight mass spectrometer (TripleTof 5600, ABSciex, Framingham, MA) equipped with a Digital PicoView ESI source (New Objective, Woburn, MA). Peptides were resolved on a 25 μm analytical column packed with 100 cm 5 μm monitor C18 and introduced to the mass spectrometer at a flow rate of ~10 nL/min using an HPLC gradient (4-55% B in 600 min; spray voltage=2800V) (Zhou et al., 2012). The mass spectrometer was operated in data dependent mode, with the top 50 precursors (charge state +2 to +5, >50 counts) in each MS scan (800 ms, scan range 350-1500 m/z) subjected to MS/MS (minimum time 100 ms, scan range 100-1800 m/z).

LC-MS/MS data processing for iTRAQ analysis. Data files were converted to .mgf using MSDataConverter version 4.0.404 (ABSciex) with the protein pilot peak generation algorithm, and re-calibrated using parameters derived from fitting experimentally observed masses in high confidence peptide identifications. Files were searched using Mascot version 2.2.1 against a forward-reversed human (38190 forward entries) NCBI refseq database (downloaded Nov. 2009) with an appended cRAP [common repository of adventitious proteins (Craig et al., 2006)] database of 752 entries. Precursor and product ion tolerances were both 0.5 Da. Search parameters included trypsin specificity, up to 2 missed cleavages, fixed carbamidomethylation (C), variable oxidation (M) and fixed iTRAQ modification (N-term, K). After searching, an excel spreadsheet containing the mascot search results was generated using Multiplierz version 0.8.3 (Parikh et al., 2009). Data were first processed to remove reverse database hits and forward hits with FDR >1.0%, and then to remove identifications with mass deviations greater than 25 ppm. iTRAQ reporter ion intensities were corrected for isotopic impurities as well as minor variations in source protein concentration. Abundance ratios were derived by summing reporters for all peptides mapping to unique genes across replicates, and only genes represented by 2 or more unique peptides are reported.

Determination of oxygen consumption rate (OCR) in isolated mitochondria. OCR was measured in real time using the XF24 extracellular flux analyzer instrument and the AKOS algorithm v1.5.069 software (Seahorse Bioscience Inc., Chicopee, MA). Briefly, the heavy membrane fraction containing mitochondria was prepared as above and loaded on XF24 V7 plates at 15 μg/well in 100 μL of mitochondria assay solution (MAS; 70 mM sucrose, 220 mM mannitol, 10 mM KH_2PO_4, 5 mM MgCl2, 2 mM HEPES pH 7.2, 1 mM EGTA, 0.2% defatted BSA). The plates were spun at 3400 rpm for 10 min at 4ºC. An additional 300 μl MAS was added and the plates were incubated at 37°C for 10 min in the absence of CO_2. Mitochondrial respiration was measured in different respiratory states as previously established (Chance and Williams, 1955). Briefly, OCR measurements were taken in 4 or 6 min periods with 30 s intervals between measurements for a total assay time of 37 min. State II respiration (non-phosphorylating state) was measured upon addition of glutamate/malate or succinate as respiratory substrates at 5 mM each in 100 μl MAS. Glutamate/malate donate electrons to complex I via NADH, and succinate donates electrons to complex II via $FADH_2$. Succinate was combined with 2.5 μM rotenone to inhibit the reverse flow of electrons to complex I. For measurement of state III and IV, 2 mM ADP and 4 μM oligomycin were sequentially delivered using the instrument's individual injection ports. After oligomycin administration, two additional inhibitors were consecutively injected for routine quality control assessment in all experiments.

These included 4 μM of the uncoupler FCCP to examine the maximal ETC activity rate when the electron transport was uncoupled from ATP synthesis, and 4 μM of antimycin A (AA) to inhibit the flow of electrons through complex III, preventing the oxidation of both NADH and succinate by mitochondria. See also Figures 7D and E.

Knockdown studies. The following lentiviral vectors containing short hairpins against SYK (Hahn et al., 2009) and GCS were purchased from The RNAi Consortium (TRC, the Broad Institute); SYK (TRCN0000196401 (#1), TRCN0000003163 (#3), and TRCN0000003164 (#4), GCS (TRCN0000048484 (#2) and TRCN0000048486 (#4). In all experiments, shGFP was used as control. Viral supernatants were produced according to the TRC standard protocols and used to spinfect 500,000 cells for 2 hr at 460 g. The effect of SYK knockdown on palmitate-induced basal OCR was assessed after 24 hr. The effect of GCS knockdown on cell viability was assessed after 72 hr.

For siRNA-mediated depletion of PPARγ, the following siRNAs were used; J-003436-09 (#1), J-003436-08 (#2), and J-003436-07 (#3) (ONTARGETplus, Dharmacon). $5x10^5$ cells were plated in 500 μl medium/well in a 12-well plate. For each transfection, siRNAs (final concentration 50 nM) were mixed with 18 μl Interferin transfection reagent (polyplus transfection-http://www.polyplus-transfection.com/transfection-reagents/2_rna-interference/1_sirna_tranfection/sirna-transfection-interferin/) in 50 μl OPTI-MEM (Life Technologies). The mixture was vortexed for 10 s and incubated at room temperature for 10 min. The mixture was then added dropwise to the cells and the plate was gently swirled. On the following day, 500 μl of cell culture medium was added. Cell viability and knockdown efficiency was assessed 72 hr after transfection.

Analysis of ^{13}C-labelled metabolites. Cell pellets were lysed in methanol:water (1:1 v/v) via 3 cycles of freeze-thawing. The resulting extraction mixture was vortexed for 30 min and insoluble debris were removed by centrifugation. The supernatants were taken for LC-MS analysis. Intracellular and media ^{13}C-labelled intermediates were quantified using LC-MS/MS with an API4000 triple quadruple MS system (AB Sciex, Framingham, MA). Analytes of interests were individually tuned and the most sensitive MRM was selected for each analyte. Waters Acquity UPLC HSS T3 2.1x100 mm, 1.8 μm was used for all LC-MS/MS analysis. For TCA cycle intermediates, 5 mM dibutylamine acetate was used as mobile phase A and acetonitrile was mobile phase B. A gradient of 6 min at 0.20 mL/min from 1% to 30% of mobile phase B was employed. Amino acids were prepared for analysis using the AccQ-fluor reagent kit (Waters Corp, Milford, MA). The derivatized amino acids were separated on the Waters Acquity UPLC

HSS T3 2.1x100mm, 1.8 µm column with a 13.5 min gradient from 2% to 30% acetonitrile with 0.1% formic acid. The mobile A phase was 0.1% formic acid in water. For the measurement of media $U^{13}C$-glucose a three fold excess of acetonitrile was added to the conditioned media. The per-*O*-trimethylsilyl-*O*-methyl derivative of $U^{13}C$-glucose was generated using methoxamine (MOX) reagent and BSTFA in 1% TMCS (Thermo Fisher Scientific, Pittsburgh PA). Derivatized $U^{13}C$-glucose was measured by capillary GC/MS using Finnigan trace ultra gas chromatograph interfaced to a Finnigan trace DSQ mass spectrometer (Austin, TX). GC was performed on an Restek Rtx-5Sil MS capillary column (15 m X 0.25 mm i.d., 0.25 µm film thickness; flow-rate 1.0 ml/min He carrier gas; column temperature 70°C for 1 min, programmed to 300°C at 20°C per min, held for 2 min). Mass spectra were obtained in single-ion monitoring (SIM) mode (323.2 *m/z*). At least three separate injections were measured per sample and the percent enrichment of ^{13}C-labeled metabolites in the total metabolite pool was calculated for each metabolite. To facilitate comparison across a panel of eight cell lines and independent experiments, mean values for ^{13}C enrichment were determined for all OxPhos and BCR cell lines, and these means were normalized to the composite mean percent enrichment of the four BCR cell lines.

Palmitate treatment and proliferation assays. Cells were grown in amino acid-free and serum-free RPMI medium supplemented with amino acids except L-glutamine to final concentrations as in RPMI standard culture medium. This medium was subsequently supplemented with either 0.5 mM carnitine alone or in combination with 0.2 mM palmitate. Cell proliferation was analyzed using the ClickIT EdU Flow Cytometry Assay kit (Invitrogen) following manufacturer's instruction.

Lactate measurements. Lactate was measured using the Synchron Systems lactate reagent kit per manufacturer's instructions (Beckman Coulter). To derive the portion of lactate produced by glycolysis, cells were seeded exactly as they were in the whole cell respirometry assays and treated with 2.5 µm oligomycin, 20 mM 2-deoxyglucose (2DG), or 10 mM oxamate (Rodriguez-Enriquez et al., 2008) for 2 hr at 37°C prior to sample collection. Glycolytically-derived lactate was defined as the difference between lactate produced in the presence and absence of glycolytic inhibitors.

Pyruvate dehydrogenase enzyme activity assays. PDH activity was assessed in isolated mitochondria (100 µg) from each DLBCL cell line in 5-6 independent experiments using a microplate assay kit (MitoSciences, Eugene, OR) per manufacturer's instructions.

Analysis of cellular ATP content, mitochondrial ATP synthesis, and energy budget calculations. ATP content was measured using the CellTiter Glo Luminescent Assay per manufacturer's instructions (Promega, Fitchburg, WI). The rate of mitochondrial ATP synthesis was determined as previously described (Shepherd et al., 2006). Briefly, $2.5x10^5$ cells were resuspended in 1 ml of buffer containing 150 mM KCl, 25 mM Tris-HCl, 2 mM EDTA, 0.1% BSA, 10 mM K_3PO_4, 0.1 mM $MgCl_2$, 40 μg/ml digitonin, 0.15 mM P_1,P_5-Di(adenosine) pentaphosphate (an inhibitor of adenylate kinase), 10 mM malate, 10 mM pyruvate, and 1 mM ADP, with or without 1 μM oligomycin. Cells were incubated at 37°C for 15 min. At 0, 5, 10, and 15 min, 50 μl aliquots of the reaction mixture were quenched in 450 μl of boiling buffer containing 100 mM Tris-HCl and 4 mM EDTA (pH 7.75) for 2 min. The aliquots were then diluted 1/10 in the quenching buffer and the quantity of ATP determined using the CellTiter Glo. The rate of mitochondrial ATP synthesis was calculated from the difference in ATP content in the presence and absence of oligomycin. Each sample was analyzed in triplicate, with two to three independent experiments for each cell line.

For energy budget calculations, the contribution of mitochondria and glycolysis to total cellular ATP was measured as previously reported (Guppy et al., 2002). Briefly, oxidative ATP turnover was calculated assuming a P/O ratio of 2.36, where P is nmol of ATP produced per nmol of oxygen consumed (O), which was in turn derived from the oligomycin-sensitive portion of OCR. The contribution of glycolysis to energy budget was calculated assuming a 1:1 stoichiometric ratio between glycolytically-derived lactate (as described above) and glycolytically-derived ATP. OCR and lactate measurements were done over a 2 hr period. For each cell line, nmol of ATP derived from glycolysis or oxidative phosphorylation were then pooled and percent contributions to the total ATP production were calculated.

Measurement of mitochondrial content in DLBCL cell lines. $1x10^6$ cells per cell line were washed once with warm HBSS (with Ca^{2+} and Mg^{2+}). Cells pellets were resuspended in 1 ml of HBSS solution containing 200 nM MitoTracker Red (Invitrogen) and 40 μM verapamil (Sigma) and incubated at 37°C for 15 min. After labeling, cells were washed once with HBSS and resuspended in 1 ml of fresh HBSS. The mean fluorescence intensity at 581 nm was analyzed by flow cytometry for each cell line.

Assessment of mitochondrial superoxide, total Cellular ROS levels and GSH content. Steady state and antimycin A-induced mitochondrial superoxide levels were assessed using MitoSOX Red (Molecular Probes) and the ratio of induced to steady state values determined. Throughout these measurements, the effect of mitochondrial membrane potential ($\Delta\Psi_m$) on

mitochondrial accumulation of MitoSOX Red was taken into account. Briefly, for steady state mitochondrial ROS measurements, $1x10^6$ cells were washed with HBSS buffer containing Mg^{2+} and Ca^{2+} and incubated for 15 min at 37°C in 1 ml of HBSS solution containing 5 µM MitoSOX Red and 40 µM verapamil (Sigma) to ensure stable maintenance of MitoSOX Red content within cells. In parallel cell samples, $\Delta\Psi_m$ was analyzed using 50 nM tetramethylrhodamine, ethyl ester (TMRE; Molecular Probes) in the presence of 40 µM verapamil in normal culture media at room temperature for 60 min. MitoSOX Red and TMRE intensities were then assessed using flow cytometry. MitoSOX Red intensity values were normalized to TMRE intensity values. For assessment of ROS levels induced by antimycin A, similar measurements were performed in the presence of 1 µM antimycin A (Sigma). The ratio of induced/steady state was calculated in multiple independent experiments using four independent cell lines per DLBCL subtype ran in triplicate and the mean of pooled values per DLBCL subtype was determined.

Total cellular ROS levels were measured using 5-(and-6)-chloromethyl-2',7'-dichlorodihydrofluorescein diacetate, acetyl ester (CM-H_2DCFDA, Molecular Probes). Briefly, $1x10^6$ cells were washed and incubated in PBS containing 2 µM CM-H_2DCFDA and 40 µM verapamil for 60 min at 37°C. Cells were then resuspended in normal media and incubated for an additional 15 min before flow cytometry measurement. Parallel positive control samples included cells treated with 50 µM tert-butylhydroperoxide, a potent inducer of ROS.

GSH content was measured using a glutathione assay kit (Northwest Life Science Specialties, LLC) per manufacturer's instruction and used to derive GSH concentration.

SUPPLEMENTAL REFERENCES

Chance, B., and Williams, G. R. (1955). Respiratory enzymes in oxidative phosphorylation. I. Kinetics of oxygen utilization. J Biol Chem *217*, 383-393.

Craig, R., Cortens, J. C., Fenyo, D., and Beavis, R. C. (2006). Using annotated peptide mass spectrum libraries for protein identification. J Proteome Res *5*, 1843-1849.

Ficarro, S. B., Zhang, Y., Lu, Y., Moghimi, A. R., Askenazi, M., Hyatt, E., Smith, E. D., Boyer, L., Schlaeger, T. M., Luckey, C. J., and Marto, J. A. (2009). Improved electrospray ionization efficiency compensates for diminished chromatographic resolution and enables proteomics analysis of tyrosine signaling in embryonic stem cells. Anal Chem *81*, 3440-3447.

Hahn, C. K., Berchuck, J. E., Ross, K. N., Kakoza, R. M., Clauser, K., Schinzel, A. C., Ross, L., Galinsky, I., Davis, T. N., Silver, S. J.*, et al.* (2009). Proteomic and genetic approaches identify Syk as an AML target. Cancer Cell *16*, 281-294.

Kloo, B., Nagel, D., Pfeifer, M., Grau, M., Duwel, M., Vincendeau, M., Dorken, B., Lenz, P., Lenz, G., and Krappmann, D. (2011). Critical role of PI3K signaling for NF-kappaB-dependent survival in a subset of activated B-cell-like diffuse large B-cell lymphoma cells. Proc Natl Acad Sci U S A *108*, 272-277.

Parikh, J. R., Askenazi, M., Ficarro, S. B., Cashorali, T., Webber, J. T., Blank, N. C., Zhang, Y., and Marto, J. A. (2009). multiplierz: an extensible API based desktop environment for proteomics data analysis. BMC Bioinformatics *10*, 364.

Rodriguez-Enriquez, S., Gallardo-Perez, J. C., Aviles-Salas, A., Marin-Hernandez, A., Carreno-Fuentes, L., Maldonado-Lagunas, V., and Moreno-Sanchez, R. (2008). Energy metabolism transition in multi-cellular human tumor spheroids. J Cell Physiol *216*, 189-197.

Shepherd, R. K., Checcarelli, N., Naini, A., De Vivo, D. C., DiMauro, S., and Sue, C. M. (2006). Measurement of ATP production in mitochondrial disorders. J Inherit Metab Dis *29*, 86-91.

Zhou, F., Lu, Y., Ficarro, S. B., Webber, J. T., and Marto, J. A. (2012). Nanoflow Low Pressure High Peak Capacity Single Dimension LC-MS/MS Platform for High-Throughput, In-Depth Analysis of Mammalian Proteomes. Anal Chem *84*, 5133-5139.